Tuning the ICON-A 2.6.4 Climate Model with Machine-learning based Emulators and History Matching

Pauline Bonnet[1,*], Lorenzo Pastori[1,*], Mierk Schwabe[1], Marco Giorgetta[2], Fernando Iglesias-Suarez[1], and Veronika Eyring[1,3]

[1]Deutsches Zentrum für Luft- und Raumfahrt (DLR), Institut für Physik der Atmosphäre, Oberpfaffenhofen, Germany
[2]Max Planck Institute for Meteorology Hamburg (Germany)
[3]University of Bremen, Institute of Environmental Physics (IUP), Bremen, Germany
[*]These authors contributed equally to this work.

Correspondence: Pauline Bonnet (pauline.bonnet@dlr.de) and Lorenzo Pastori (lorenzo.pastori@dlr.de)

Abstract. In climate model development, *tuning* refers to the important process of adjusting uncertain free parameters of subgrid-scale parameterizations to best match a set of Earth observations such as global radiation balance or global cloud cover. This is traditionally a computationally expensive step as it requires a large number of climate model simulations. This step also becomes more challenging with increasing spatial resolution and complexity of climate models. In addition, the manual tuning relies strongly on expert knowledge and is thus not independently reproducible. To reduce subjectivity and computational demands, Machine Learning (ML)-based tuning methods have become an active research subject. Here we build on these developments and apply ML-based tuning to the atmospheric component of the Icosahedral Nonhydrostatic Weather and Climate Model (ICON) at 80 km resolution. Our approach follows a workflow similar to other proposed ML-based tuning methods: (1) creating a Perturbed Parameter Ensemble (PPE) of limited size with randomly selected parameters, (2) fitting an ML-based emulator to the PPE to generate a large emulated ensemble with the emulator, and (3) shrinking the parameter space to regions compatible with observations, using a method inspired by history matching. However, in contrast to previous works, we apply a sequential approach: the selected set of tuning parameters is updated in successive phases depending on the results of a sensitivity analysis with Sobol indices. We tune for global radiative, cloud properties, zonal wind velocities and wind stresses on the ocean surface. With one iteration of this method, we achieve a model configuration yielding a global top-of-atmosphere net radiation budget in the range of $[0, 1]$ W/m^2, and global radiation metrics and water vapor path consistent with the reference observations. Furthermore, the resulting ML-based emulator allows us to identify the parameters that most impact the outputs that we target with tuning. The parameters that we identified as mostly influential for the physics output metrics are the critical relative humidity in the upper troposphere and the conversion coefficient from cloud water to rain, influencing the radiation metrics and global cloud cover, together with the coefficient of sedimentation velocity of cloud ice, having a strong non-linear influence on all the physics metrics. The existence of non-linear effects further motivates the use of ML-based approaches for parameter tuning in climate models.

1 Introduction

Climate and Earth system models are developed and continuously improved to understand the behaviour of the Earth system and to project climate change (Tebaldi et al., 2021). Due to their complexity as well as constraints on computational resources, the resolution of climate models is relatively coarse, so that a number of key processes occur on scales smaller than the model grid scale. These non-resolved processes, such as convection, radiation, turbulence, cloud microphysics, and gravity waves, are described statistically for each grid cell through so-called parameterizations, which are a cause of biases and uncertainties in climate projections (Gentine et al., 2021) due to uncertainties in their formulation and in the selection of the underlying free parameters. To constrain the values of the free parameters involved in the parameterizations, tuning is an important step in the development of climate models (Hourdin et al., 2017), where these parameters are adjusted such that the outputs of the climate model reproduces the observed states of the Earth system reasonably well.

Model tuning is typically a very time-consuming and computationally expensive step. It has to be conducted for all components of a climate model (such as atmosphere, ocean and land) and for the coupled model (see for instance the tuning of the coupled ICON Earth System Model by Jungclaus et al. (2022)).

Traditionally, tuning in climate models is done manually, i.e., the parameters are changed individually (or few at a time) in a sequential manner, with expert knowledge guiding the successive choices in the tuning of the parameters (Hourdin et al., 2017; Mauritsen et al., 2012; Schmidt et al., 2017; Giorgetta et al., 2018; Mignot et al., 2021). Such manual approaches may retain some form of subjectivity, and are therefore hard to replicate. There is also the risk of neglecting interactions among the processes affected by the changed parameters, which may lead to compensating errors, e.g., a model's low climate sensitivity might be paired with weak aerosol cooling, resulting in an apparent match with historical data but potentially inaccurate future projections (see e.g. Fig. 3 of Hourdin et al. (2017)).

In this work we investigate how machine learning (ML) techniques can help addressing the aforementioned challenges faced in model tuning, using the atmospheric component of the ICON model (Giorgetta et al., 2018) as an example. In recent years, ML-based *automatic* tuning methods have been widely investigated. These methods intend to tune the climate models in fewer manual steps for the user compared to fully manual approaches, and aim to improve the accuracy and reproducibility of parameter tuning by giving it a mathematical formulation amenable to numerical treatment. The goal is to find the regions of parameter space for which the model outputs are consistent with observation-based reference datasets, where consistency is defined on a suitably-defined distance between outputs and observations and accounts for a tolerance given by observational uncertainties and model structural errors. A number of mathematical tools have been developed to tackle inverse problems such as model tuning. The one we focus on in this work belongs to the family of Bayesian approaches (this is not the only possible choice, and refer to (Zhang et al., 2015) for more details on other possibilities). In a Bayesian setting, this is achieved by an iterative and efficient exploration of the space of the parameters being tuned, which is enabled by the construction of an ML-based surrogate or emulator of the climate model that aims at approximating the climate model outputs at much cheaper computational costs. In its most general formulation, this procedure consists of iterating the following steps: (1) generate a perturbed parameter ensemble (PPE), i.e., an ensemble of climate model simulations obtained by sampling configurations of

tuning parameters within the valid parameter ranges, (2) train a computationally cheap ML-based emulator on the PPE output to approximate the parameter-to-output relationship, and (3) use the emulator for a denser sampling of the parameter space, and shrink the space of allowed parameter configurations to the most promising one, i.e., the parameters most likely yielding a tuned version of the climate model. A commonly adopted method for selecting promising parameter configurations is history

60   matching (Williamson et al., 2013, 2017). History matching aims at minimizing the number of required model simulations in the search of acceptable parameters, by balancing the sampling of unexplored parameter regions with the sampling close to configurations found potentially compatible with observations. This is achieved using a metric that weights both the distance of the emulator predictions from the observational references (small meaning close to observationally-compatible configurations), and the uncertainty of the emulator (high in unobserved parameter regions). The three steps described above are repeated until

65   the model outputs used as tuning metrics converge to the corresponding observational range, thus yielding one or multiple tuned parameter configurations, or a distribution thereof (Watson-Parris et al., 2021).

Several implementations of the ideas above have been proposed, for tuning models of different complexity. History matching has been implemented to constrain parameters in the coupled climate model (HadCM3) (Williamson et al., 2013) and to estimate parametric uncertainty in the NEMO ocean model (Williamson et al., 2017). It has also been used to tune parameters

70   of the turbulence scheme of a single column model version of ARPEGE-Climat 6.3, using large-eddy simulations as reference (Couvreux et al., 2021). History matching in combination with single-column models was also employed to constrain convective parameters for their subsequent use in the LMDZ atmospheric model of the IPSL Earth System Model (Hourdin et al., 2021). Furthermore, Hourdin et al. (2023) showed another successful application to the IPSL model, finding an ensemble of tuned parameter configurations as good as the manually tuned vesion IPSL-CM6A-LR used for CMIP6. Besides their use

75   in history matching, ML-based emulators find applications in parameter tuning also in combination with ensemble methods (Cleary et al., 2021) (with test applications on Lorenz '63 and '96 models (Cleary et al., 2021), convection schemes in idealized global circulation model (Dunbar et al., 2021), gravity waves parameterizations (Mansfield and Sheshadri, 2022)), and with approximate Bayesian computation (Watson-Parris et al., 2021).

Building on these previous tuning efforts, here we design a tuning approach assisted by history matching for the atmospheric

80   component of the Icosahedral Nonhydrostatic Weather and Climate Model (ICON-A version 2.6.4) (ICON, 2015; Zängl et al., 2014). The model's icosahedral grid has a resolution of approximately 80 km (*R2B5* grid), offering an improvement in spatial detail compared to previous applications of these tuning approaches in global climate models. For instance, Williamson et al. (2013) used a resolution of 96 x 73 grid points in latitude and longitude (approximately 417 km x 278 km at the equator), while Hourdin et al. (2021, 2023) utilized 144 x 143 grid points (approximately 160 km at the equator). From an algorithmic

85   perspective, a further distinctive feature of our ICON-A tuning method is that we incorporate history matching in a sequential approach, where we separate tuning into phases in which different sets of tuning parameters are sequentially constrained with history matching. This approach reduces the number of parameters being tuned in each phase, and allows us to reduce the required size of the PPEs, and therefore the computational costs, which is particularly relevant given the total number of tuning parameters and the relatively high resolution (approx. 80 km) we target here. In our sequential approach we first focus on

90   global radiative and cloud properties, referred to as *physics* outputs (Giorgetta et al., 2018), and then on outputs related to

atmospheric circulation properties, referred to as *dynamics* outputs (Giorgetta et al., 2018). For the physics tuning we apply history matching in the sequential manner explained before, and show that the ICON-A physics outputs converge towards observational references in a few iterations. The ML-based tuning of the physics outputs serves as the basis for the second step targeting the dynamics outputs. For this step we follow the approach of Giorgetta et al. (2018) by generating a PPE and selecting the best performing model configurations, where our criterion for evaluating the model's performance keep the highest priority on achieving a nearly balanced global annual net radiation flux at top of the atmosphere (TOA) while aiming to achieve a high performance on the dynamics outputs. Our results are compared to the manually tuned version of the ICON-A model that was presented in Giorgetta et al. (2018) and Crueger et al. (2018), with a grid size of approximately 160 km (*R2B4* grid), which is two times coarser than the resolution we focus on in this paper (grid size of approximately 80 km, *R2B5* grid). In the remainder of the paper, we refer to this manually tuned ICON version as *ICON-aes-1.3*.

The article is organized as follows. We first introduce the ICON-A model, the ML-based tuning method and the reference datasets used in this study in Section 2. We then present the results of the ML-based tuning approach for ICON-A in Section 3, an evaluation of our selected runs in Section 4, and conclude in Section 5, where we also discuss the potential issues of our proposed approach and an outlook on how to possibly overcome them.

2 Methods

2.1 ICON-A modelling framework

The Icosahedral Nonhydrostatic Weather and Climate Model (ICON) is a modelling framework for Climate and Numerical Weather prediction developed jointly by the German Weather Service (DWD) and the Max Planck Institute for Meteorology (MPI-M) (ICON, 2015; Zängl et al., 2014). We use ICON's atmospheric component (ICON-A) (Zängl et al., 2014; Giorgetta et al., 2018), version 2.6.4, and conduct AMIP experiments with the icosahedral grid *R2B5* (≈ 80 km in the horizontal, for details see Table 1 in Giorgetta et al. (2018)) with an implicitly coupled land model. The top height of the atmospheric model is 83 km with 47 full vertical levels and numerical damping starting at 50 km. Subgrid-scale processes are described by parameterizations and include radiative effects, moist convection, vertical diffusion, cloud microphysics, cloud cover, and orographic and non-orographic gravity waves (Giorgetta et al., 2018). The time steps used in the model simulations are one hour for the radiation scheme and six minutes for the atmospheric scheme. For our PPEs we run ICON-A for one year spin up (1979) and then for one year for tuning physics outputs (1980). We then run the model for one year spin up (1979) and then for ten years (1980-1989) for the dynamics outputs, as described in the following sections.

2.2 Parameters and Outputs

The first step to ML-based tuning, as for manual tuning, is to select the tuning parameters and output metrics that are to be fitted. Our choice of the metrics is informed by the manual tuning of the ICON model by Giorgetta et al. (2018) and Crueger et al. (2018). There, the authors worked on model versions preceding ICON-aes-1.3.00, which resulted from their work, with

Physics outputs metrics	Spatial average	Averaging period	Reference datasets	Target range
TOA net shortwave (SW) radiation (rsdt-rsut)	Global (references and PPEs)	1980	Giorgetta et al. (2018)	[240, 241] W/m^2
TOA net longwave (LW) radiation (rlut)	Global (references and PPEs)	1980	Giorgetta et al. (2018)	[-241, -240] W/m^2
TOA radiation balance (rsdt-rsut-rlut)	Global (references and PPEs)	1980	Giorgetta et al. (2018)	[0, 1] W/m^2
Cloud cover (clt)	Global (references and PPEs)	1982-1991 1980-1989 (1980 for PPEs)	CLARA-AVHRR V002 ESACCI-Cloud AVHRR-AMPM-fv3.0	62.7 % 65.1 %
Water vapor path (prw)	Global (references and PPEs)	1980-1989 (1980 for PPEs)	ERA5	[24.1] kg/m^2

Table 1. Physics outputs together with respective observational datasets (CERES-EBAF (NASA/LARC/SD/ASDC, 2019) and ERA5 (Dee et al., 2011)) and target ranges used in this work. All the outputs in this table are globally averaged (for both the reference datasets and the ICON-A simulations we conduct). The averaging period used for both reference datasets and our simulations (PPEs) is reported in the third column. TOA stands for "top of the atmosphere".

Dynamics Output metrics	Spatial average	Averaging period	Reference datasets	Target range
Zonal wind velocity (ua)	60° North at 10 hPa (references and PPEs)	1980-1989 (references and PPEs)	ERA5, MERRA2, ERA-Interim	(10.94, 11.15, 10.94) m/s
Zonal wind velocity (ua)	60° South at 10 hPa (references and PPEs)	1980-1989 (references and PPEs)	ERA5, MERRA2, ERA-Interim	(32.77, 34.03, 33.15) m/s
Surface downward eastward wind stress (tauu)	North-Atlantic Ocean (NAO) (references and PPEs)	1980-1989 (references and PPEs)	ERA5, MERRA2, ERA-Interim	(2.947e-3, 5.395e-3, 3.645e-3) N/m^2
Surface downward eastward wind stress (tauu)	Southern Ocean (SOO) (references and PPEs)	1980-1989 (references and PPEs)	ERA5, MERRA2, ERA-Interim	(0.1367, 0.1413, 0.1359) N/m^2

Table 2. Dynamics outputs together with respective observational datasets (ERA5 (Hersbach et al., 2020)) used in this work. The North Atlantic Ocean (NAO) region and the Southern Ocean (SOO) region are those defined in the AR6 database (Iturbide et al., 2020).

a coarser resolution R2B4 of $\approx 160\,\mathrm{km}$, 47 vertical layers resolving the atmosphere up to a height of $83\,\mathrm{km}$, and time steps of two hours for the radiation scheme and ten minutes for the atmospheric scheme.

Table 1 reports the output metrics, and the corresponding reference datasets and values, that we focus on in this study, which represent global radiative and cloud properties and are referred to as the *physics* outputs. These physics output metrics are all global and multi-year averages. In particular, as shown in Table 1, we use the annual average over 1980 in our PPEs (apart from our last PPE, as discussed later), and compare it with the multi-year averages of the reference datasets.

The output metrics related to atmospheric circulation properties, the *dynamics* outputs, are given in Table 2. There, the zonal mean velocity at 60° North and South at 10 hPa serves as proxy for the representation of high latitude jets. This is a widely used target for evaluating simulations of the polar jets in models resolving the stratosphere (e.g. as seasonal means in Tripathi et al. (2014); Domeisen et al. (2020a, b); Rao et al. (2020); Baldwin et al. (2021)). The surface downward, eastward wind stress mean over the North Atlantic Ocean and the Southern Ocean (defined in the AR6 database Iturbide et al. (2020)) are proxies for the forcing on the ocean surface. These dynamics output metrics are multi-year averages. In particular, as shown in Table 2, we use the average over the period 1980-1989 in our PPEs, and compare it to the multi-year averages of the reference datasets reported in Table 2. We use different averaging periods for physics and dynamics outputs because of the different year-to-year variability and equilibration times of the associated variables. As substantiated in Section 3.3.1, the physics outputs have lower year-to-year variability compared to the dynamics ones, meaning that one simulated year is sufficient to obtain a representative value for the annual averages. Conversely, for dynamics metrics the annual averages need to be estimated from multi-year simulations due to their larger variability and sensitivity to geographic patterns.

Following Giorgetta et al. (2018), the parameterizations we select for tuning for the physics outputs are moist convection, vertical diffusion, cloud microphysics and cloud cover. In Table 3 we report the parameters from these parameterizations (which we therefore refer to as physics parameters) which we select for our tuning experiment. The parameterizations we select for tuning for the dynamics outputs are the orographic and non-orographic gravity waves schemes. In Table 4 we report the parameters from these parameterizations (referred to as dynamics parameters) which we select for our tuning experiment.

2.3 Reference datasets

To tune ICON-A we use reference values for the output metrics from Earth observations and reanalysis data. As in Giorgetta et al. (2018), the main goal here is *to obtain a slightly positive global annual mean downward net radiation flux at the top of the atmosphere (TOA), between 0 and 1 W/m^2, based on a net shortwave flux and an outgoing longwave radiation close to observational estimates*. For the two radiation fields (rsdt-rsut) and rlut (see Tab. 1 for definitions), the typical interval [240 W/m^2, 241 W/m^2] is used as a reference value, as estimated in (Giorgetta et al., 2018), following observational datasets (CERES-EBAF-Ed4.0, 2000-2016) and Kato et al. (2013); Loeb et al. (2009). For cloud cover, we use CLARA-AVHRR (Karlsson et al., 2020) and ESACCI-CLOUD (Stengel et al., 2017), and for the water vapour path, we use ERA5 (Hersbach et al., 2020) (see Section A for time series of these observational datasets). For the dynamics outputs, we use ERA5, ERA-Interim (Dee et al., 2011) and MERRA2 (Gelaro et al., 2017). We refer the reader to Appendix A for the time series of some of the observational products used in this work.

Physics parameters with corresponding ranges			Parameterization
Average entrainment rate for midlevel convection	entrmid	[2e-5, 3e-4]	Moist convection
Average entrainment rate for penetrative convection	entrpen	[2e-5, 6e-4]	Moist convection
Average entrainment rate for cumulus downdrafts	entrdd	[5e-5, 6e-4]	Moist convection
Characteristic adjustment time scale [s]	cmftau	[2e2, 1e4]	Moist convection
Neutral limit Prandtl number	pr0	[5e-1, 1.2]	Vertical diffusion
Critical relative humidity parameter at the upper troposphere	crt	[5e-1, 9e-1]	Cloud cover
Fractional convective mass flux across the top of cloud	cmfctop	[1e-2 , 2e-1]	Moist convection
Coefficient for determining conversion from cloud water to rain	cprcon	[1.5e-5, 3.5e-4]	Moist convection
Coefficient of autoconversion of cloud ice to snow	ccsaut	[0.2 , 4]	Cloud microphysics
Minimum in-cloud water mass mixing ratio in mixed phase clouds	csecfrl	[1.0e-5 , 1.0e-4]	Cloud microphysics
Coefficient of sedimentation velocity of cloud ice	cvtfall	[0.2 , 4]	Cloud microphysics
Critical relative humidity at surface	crs	[7.26e-1, 9.9e-1]	Cloud cover
Lower limit of scaling factor for saturation mixing ratio in layer below inversion	csatsc	[0.35, 1,05]	Cloud cover

Table 3. Tuning parameters related to physics parameterizations alongside the corresponding name in the ICON source code (second column from left), the range of values tested (third column from left), and the corresponding parameterization scheme they belong to (right column). The range of the parameters was inferred from the default value of the parameters given in the source code of ICON-A version 2.6.4.

Dynamics parameters with associated ranges			Parameterization
Coefficient for orographic gravity wave drag	gkdrag	[0.002, 0.28]	Sub-grid scale orographic effects
Coefficient for low level blocking	gkwake	[0.001, 0.09]	Sub-grid scale orographic effects
Root mean square gravity wave wind at the emission level	rmscon	[0.647, 1.079]	Atmospheric gravity wave effects
Minimum difference "SSO peak height - SSO mean height" [m]	gpicmea	[20,60]	Sub-grid scale orographic effects
Minimum standard deviation of SSO height [m]	gstd	[5,15]	Sub-grid scale orographic effects

Table 4. Tuning parameters related to dynamics parameterizations alongside the corresponding name in the ICON source code (second column from left), the range of values tested (third column from left), and the corresponding parameterization scheme they belong to (right column). SSO stands for "subgrid-scale orography".

2.4   ML-based tuning approach

Our ML-based tuning method is built on the history matching technique (Williamson et al., 2013, 2017), and follows a similar workflow as in (Couvreux et al., 2021; Hourdin et al., 2021, 2023). The goal is to find a region in the parameter space where the model outputs are compatible (within the observational uncertainty) with the observational data (observationally-compatible). In performing this exploration, history matching aims at finding a balance between exhaustively exploring, or sampling, the parameter space, and minimizing the number of samples required for it. Since in our case each sample corresponds to an
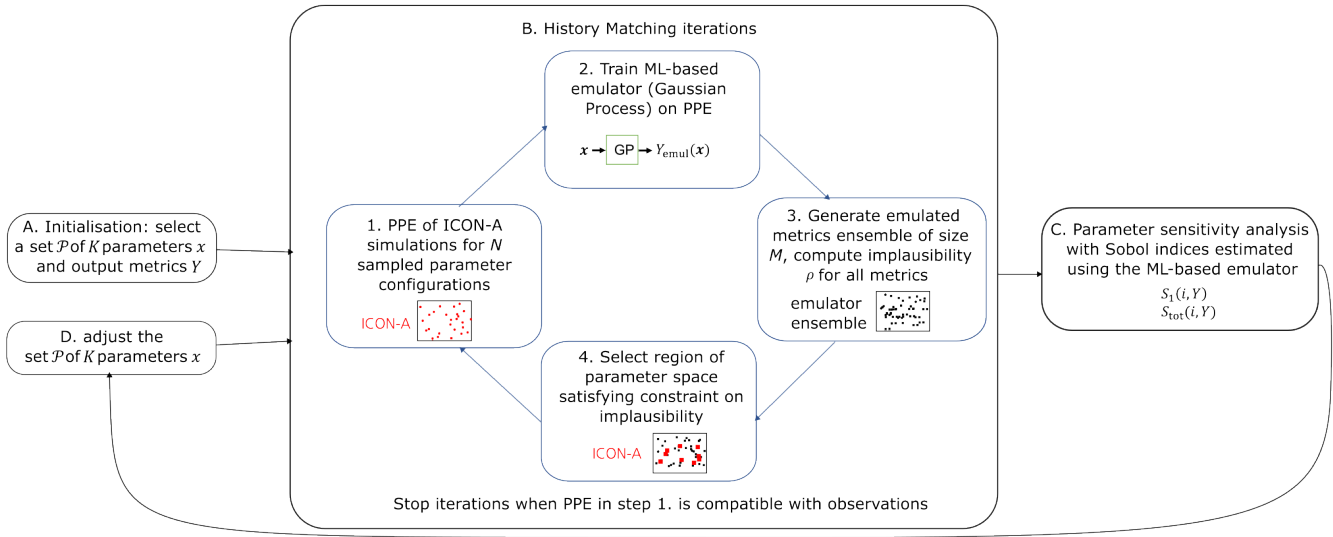
Figure 1. Schematic of the method used for the ML-based tuning of the *physics* parameters of ICON-A: history matching technique combined with a sensitivity analysis and a sequential parameter selection. The first set of tuning parameters is chosen (A), and history matching is employed to shrink the associated parameter space to an observationally-compatible region (B). If the PPEs are far from observational references, a new parameter set is chosen with the help of sensitivity analysis (C). The new parameter set (D) is used for a new phase of the tuning experiment. When one or more of the model configurations generated in the last PPE are compatible with observations, the iterations of this tuning approach stop. The model configurations compatible with observations are then evaluated.

expensive climate model simulation, we consider this method particularly well suited for our tuning task. In tuning ICON-A we embed history matching in a sequential protocol, where at each step we add or remove tuning parameters based on the outcomes of the history matching iterations. We now start by outlining the steps of the history-matching-inspired method that
165 constitutes the basis of our protocol (see also steps 1. to 4. in Fig. 1):

1. For a given set of tuning parameters $\mathcal{P}$ with K elements draw an initial Latin Hypercube (LHC) sampling of size N. Using LHC sampling, all parameters are simultaneously changed and the different samples fill the K-dimensional parameter space (within the allowed ranges specified in Tables 3 and 4) approximately uniformly. Typically, N is chosen as $N \approx 10\,K$ (Loeppky et al., 2009). Using these selected parameters, generate a PPE of ICON-A runs. The PPE consists
170 of N members, or runs, one for each sampled parameter configuration $\boldsymbol{x}_i$ (with $i = 1, ..., N$). For each run, we calculate all the output metrics described before. This results in sets of input-output training pairs $\mathcal{T}_Y = \{\boldsymbol{x}_i, Y_{\mathrm{model}}(\boldsymbol{x}_i)\}_{i=1,...,N}$, one set per output metric Y (e.g., annual average of global TOA radiation balance).

2. Fit an emulator to the generated PPE, i.e., to the training sets $\mathcal{T}_Y$ for all the output metrics Y of interest. For a given metric Y, the emulator evaluated on a configuration of tuning parameters $\boldsymbol{x}$ returns $Y_{\mathrm{emul}}(\boldsymbol{x})$, the approximation to the
175 true model output metric $Y_{\mathrm{model}}(\boldsymbol{x})$. Our choice for the model emulator is Gaussian process (GP) regression (Rasmussen

and Williams, 2005). GPs are models typically used in Bayesian regression tasks, and are very well suited for our case since (i) they have only few parameters, hence require relatively little training data for fitting, and (ii) they by construction return the uncertainty associated to their prediction, which is measured by the variance $\mathrm{Var}(Y_{\mathrm{emul}}(\boldsymbol{x}))$. This is a central quantity used in the steps below. Further details on the choice of the GP are given in Appendix B. In our implementation, we train one GP per model output.

3. Generate a large emulated metrics ensemble of size M (typically ranging from 10^5 to 10^6, here $M = 3 \times 10^5$) using the trained GP emulator. For each emulator run, calculate the implausibility measure ρ for each metric Y, with reference value Y^0 (from observations or re-analysis data) as:

$$\rho(Y_{\mathrm{emul}}(\boldsymbol{x}), Y^0) = \frac{|Y^0 - Y_{\mathrm{emul}}(\boldsymbol{x})|}{\sqrt{\mathrm{Var}(Y_{\mathrm{emul}}(\boldsymbol{x}))}} \ . \tag{1}$$

The idea behind this definition is that a small distance $|Y^0 - Y_{\mathrm{emul}}(\boldsymbol{x})|$ or a large emulator variance $\sqrt{\mathrm{Var}(Y_{\mathrm{emul}}(\boldsymbol{x}))}$ (typically true when $\boldsymbol{x}$ is far from already sampled points) will lead to a small value of ρ, hence balancing exploitation with exploration of the parameter space. Note that typically a measure of the observational uncertainty $\mathrm{Var}(Y^0)$ is included in the denominator of the implausibility measure, and defines a tolerance for assessing the convergence of history matching. This is an important distinction between traditional history matching and our implementation, which we motivate in the next point. In our case, the observational uncertainty is accounted for in the evaluation of the tuned model configurations, where we assess whether the outputs of the parameters configurations sampled with our procedure (see next points) are within the spread of the observational datasets used as reference. This is explained in Section 4.

4. Select N parameter configurations that satisfy the following constraints on the outputs (see Table 1 and Table 2 for outputs definitions):

   - $\rho(Y_{\mathrm{emul}}(\boldsymbol{x}), Y^0) < \rho_1$: for the three physics metrics TOA shortwave radiation, TOA longwave radiation, and TOA net incoming radiation,

   - $\rho(Y_{\mathrm{emul}}(\boldsymbol{x}), Y^0) < \rho_2$: for the two other physics metrics cloud cover and liquid water path, and the five dynamics metrics.

   The choice of a smaller threshold for the three radiation metrics is necessary in order to give a higher weight to the constraint on a balanced TOA radiation than on the other metrics. We use $\rho_2 = 2\rho_1$. The value of ρ_1 is automatically adjusted in order to select only N parameter sets out of the ensemble of size M. Given that we are interested in drawing parameter configurations that are representative of the space of plausible tuned parameters in few iterations, our choice of the implausibility measure as in Eq. (1) provides stricter constraints on the selected parameters, with the observational means Y^0 being the target values for the corresponding metrics.

5. Back to step 1. : Generate a new PPE of size N with ICON-A for the parameter ensemble defined in the previous step, and repeat steps from 2. to 4.

The iterations stop when one of the model configurations generated in the PPEs is compatible with observations, or when a new set $\mathcal{P}$ of tuning parameters is used. Compatibility with observations is defined based on a weighted distance of the model output metrics from their reference value, with a tolerance given by the corresponding observational uncertainty. The highest weight is given to the global TOA net radiation balance, our main tuning goal. In general, in the earlier iterations of history matching, not all the members of the next round are expected to be compatible with the observational references. The configurations that are found compatible with observations are considered representative of the space of plausible tuned parameters, and are subsequently evaluated on additional evaluation metrics to assess their quality as tuned configurations (see Section 4). The parameter set $\mathcal{P}$ is changed when the spread of the PPE generated in the last history matching iteration is too far from the observational range. The new parameter set consists of new tuning parameters together with the most influential parameters from the previous $\mathcal{P}$, for better steering the model outputs towards the observational references. The influence of the parameters on the model outputs is estimated performing an emulator-based sensitivity analysis with Sobol indices, the details of which are provided in Section 3.2.2. This results in a sequential tuning approach, integrating history matching as its core component for constraining the parameters in the sets $\mathcal{P}$ selected in the different phases. This is schematically shown in Fig. 1.

This sequential approach incorporating the previously explained history-matching-inspired method is used for the tuning of the physics outputs. The resulting model configuration serves then as basis for the next step which is the simultaneous tuning of physics and dynamics parameters and metrics. Also in this case we use a sensitivity analysis to select which physics parameters to keep in this next tuning step. In this step for the tuning of physics and dynamics parameters and metrics, we follow the manual tuning approach of (Giorgetta et al., 2018). We generate a PPE and select the best performing model configurations, where our criterion for evaluating the model's performance keeps the highest priority on achieving a nearly balanced global annual net radiation flux at top of the atmosphere (TOA). Separating the tuning of physics-only metrics from that involving also dynamics outputs allows us to use different durations of the ICON-A simulations for the two steps, and to further reduce the computational costs. Specifically, as substantiated in Section 3.3.1, the physics outputs have lower year-to-year variability and shorter equilibration timescales compared to the dynamics outputs. This means that for physics outputs shorter simulations are needed for obtaining a representative value for the annually averaged variables used as metrics.

Finally, before moving on to the results section, a technical note on the construction and evaluation of the GP emulators: we implement the GP emulator in Python using scikit-learn (https://scikit-learn.org/stable/), and used the built-in routines to optimize the GP parameters at each iteration of the above procedure (see details in Appendix B). In this work, we measure the performance of the GP regression model via the R^2 value, which for a given output Y is defined as:

$$R^2(Y) = 1 - \frac{\overline{(Y_{\text{emul}} - Y_{\text{model}})^2}}{\text{Var}(Y_{\text{model}})} \, , \tag{2}$$

where $\overline{(Y_{\text{emul}} - Y_{\text{model}})^2}$ denotes the mean squared error of the emulator over a set of testing parameters, and $\text{Var}(Y_{\text{model}})$ the variance of the true model output over the same test set.

3 Results

3.1 Summary of the generated PPEs

The PPEs generated in this work are summarized in Table 5. PPE_1 to PPE_4 are generated for the tuning of the physics output metrics from single-year ICON-A runs (1980) after a one year spin-up. PPE_1 is generated from an LHC sampling of size 30 on the (physics) parameter set:

$$\mathcal{P}_{p1} = \{\,\text{entrpen, entrmid, entrdd, cmftau, crt, pr0}\,\}\,, \tag{3}$$

which are the physics parameters used in (Giorgetta et al., 2018). PPE_2 is produced by applying history matching on the results of PPE_1. After PPE_2 a new phase of our sequential approach starts: for PPE_3 we perform a new LHC sampling on a modified parameter set:

$$\mathcal{P}_{p2} = \{\,\text{cmfctop, cprcon, ccsaut, csecfrl, cvtfall, crt, pr0}\,\}\,, \tag{4}$$

in order to increase the globally averaged cloud cover, which is consistently lower than the observational references in PPE_1 and PPE_2. The parameters in $\mathcal{P}_{p2}$ were selected among those that in the ICON-A manual tuning history (unpublished) were deemed most influential for cloud cover. Our criterion to decide which parameters to keep from $\mathcal{P}_{p1}$ to $\mathcal{P}_{p2}$ follows from the sensitivity analysis based on Sobol indices, which we present later in Section 3.2.2. Specifically, the parameters crt and pr0 associated to higher first and total Sobol indices for the cloud and water vapour metrics have been kept from $\mathcal{P}_{p1}$ to $\mathcal{P}_{p2}$. For generating PPE_3 and PPE_4, the values of the parameters in $\mathcal{P}_{p1}$ that are not present in $\mathcal{P}_{p2}$ are fixed to their best value from PPE_2 (see the right column of Table 5 and the magenta star in Fig. 2 and Fig. 3). The set $\mathcal{P}_{p2}$ is used to generate PPE_3, consisting of 30 samples sampled with LHC sampling. PPE_4 is produced by applying history matching on the results of PPE_3. The sizes of the PPEs are chosen to be smaller than the typical value of ten times the number of parameters (six parameters in $\mathcal{P}_{p1}$ and seven parameters in $\mathcal{P}_{p2}$) (Loeppky et al., 2009). This size allows a lower computational cost while being large enough to train an emulator that allows convergence of the PPEs towards reference observations, as explained in the next section 3.2.1.

In PPE_5 we then address also the tuning of dynamics outputs by varying physics and dynamics parameters simultaneously in the parameter set:

$$\mathcal{P}_{pd} = \{\,\text{entrmid, cvtfall, crt, crs, csatsc, rmscon, gkdrag, gkwake, gpicmea, gstd}\,\}\,, \tag{5}$$

and keeping the other parameters fixed to their best values in PPE_2 (see the right column of Table 5 and the magenta star in Fig. 2 and Fig. 3). Also for $\mathcal{P}_{pd}$ we follow the same strategy and keep the parameters having the highest influence on the radiation and water metrics, as can be seen from the Sobol analysis in Section 3.2.2, with the addition of crs and csatsc after further advice from ICON experts. The parameters rmscon, gkdrag and gkwake are the same dynamics parameters used in (Giorgetta et al., 2018), and we added gpicmea and gstd following advice from ICON expert knowledge. PPE_5 consists of ten-year ICON-A simulations from 1980 to 1989 (after a one year spin-up).

PPE	Parameters changed	Size	Description	Outputs	Fixed parameters
PPE_1	$\mathcal{P}_{\text{p1}} = \{\text{entrpen, entrmid,}$ entrdd, cmftau, $\text{crt, pr0}\}$	30	LHC sampling of $\mathcal{P}_{\text{p1}}$	physics	cmfctop (0.1), cprcon (2.5e-4), ccsaut (2.0), csecfrl (1.5e-5), cvtfall (2.5), csatsc (0.7), crs (0.968) (fixed from default configuration)
PPE_2	$\mathcal{P}_{\text{p1}}$	29	History matching from PPE_1	physics	
PPE_3	$\mathcal{P}_{\text{p2}} = \{\text{cmfctop, cprcon,}$ ccsaut, csecfrl, $\text{cvtfall, crt, pr0}\}$	30	LHC sampling of $\mathcal{P}_{\text{p2}}$	physics	entrpen (9.295e-5), entrmid (2.2504e-4), entrdd (1.766e-4), cmftau (2114.6), csatsc (0.7), crs (0.968) (fixed from best conf. in PPE_2)
PPE_4	$\mathcal{P}_{\text{p2}}$	30	History matching from PPE_3	physics	
PPE_5	$\mathcal{P}_{\text{pd}} = \{\text{entrmid, cvtfall, crt,}$ $\text{crs, csatsc, rmscon,}$ gkdrag, gkwake, $\text{gpicmea, gstd}\}$	80	LHC sampling of $\mathcal{P}_{\text{pd}}$	physics and dynamics	entrpen (9.295e-5), entrdd (1.766e-4), cmftau (2114.6), pr0 (0.93168), ccsaut (2.0), csecfrl (1.5e-5) (fixed from best conf. in PPE_2)

Table 5. Summary of perturbed parameters ensembles (PPEs) generated in this work. The PPEs have been sequentially generated from 1 to 5. PPE_3 is obtained from an LHC sampling of parameter set $\mathcal{P}_{\text{p2}}$, where the parameters in $\mathcal{P}_{\text{p1}}$ not included in $\mathcal{P}_{\text{p2}}$ are kept fixed to their best values from PPE_2 (and listed in the right column), which are then used further in PPE_4 and PPE_5.

3.2 ML-based tuning of physics outputs with history matching

In this section we present the results of the tuning of the physics parameters. We start by considering PPE_1 and PPE_2. As explained before, PPE_2 is generated by applying history matching after having trained a GP emulator on the outputs of PPE_1. The constructed GP emulator in this case has a good predictive performance (measured by an average R^2 score of 0.81, as discussed in more detail in Section 3.2.1 below), and can therefore accurately guide the parameter choices for PPE_2. Thanks to this, the application of only one iteration of history matching to PPE_1 is already sufficient to generate configurations in PPE_2 that achieve a balanced TOA radiation. This is demonstrated in panel (a) of Fig. 2, which shows the net short-wave (SW) versus the net long-wave (LW) TOA radiation for PPE_1 and PPE_2. There, we can clearly see that after history matching on PPE_1, PPE_2 can achieve configurations that match or get close to the observational ranges denoted by the green triangle (and to ICON-aes-1.3). The convergence of the output metrics towards their reference values can also be observed in panel (b) of Fig. 2, for the other two physics output metrics (global cloud cover versus water vapor path) for PPE_1 and PPE_2. There, the distribution of the PPE_2 outputs is converging towards the observational references (green markers). The convergence of history matching towards the observational references can also be seen in the distribution of the sampled parameters for the
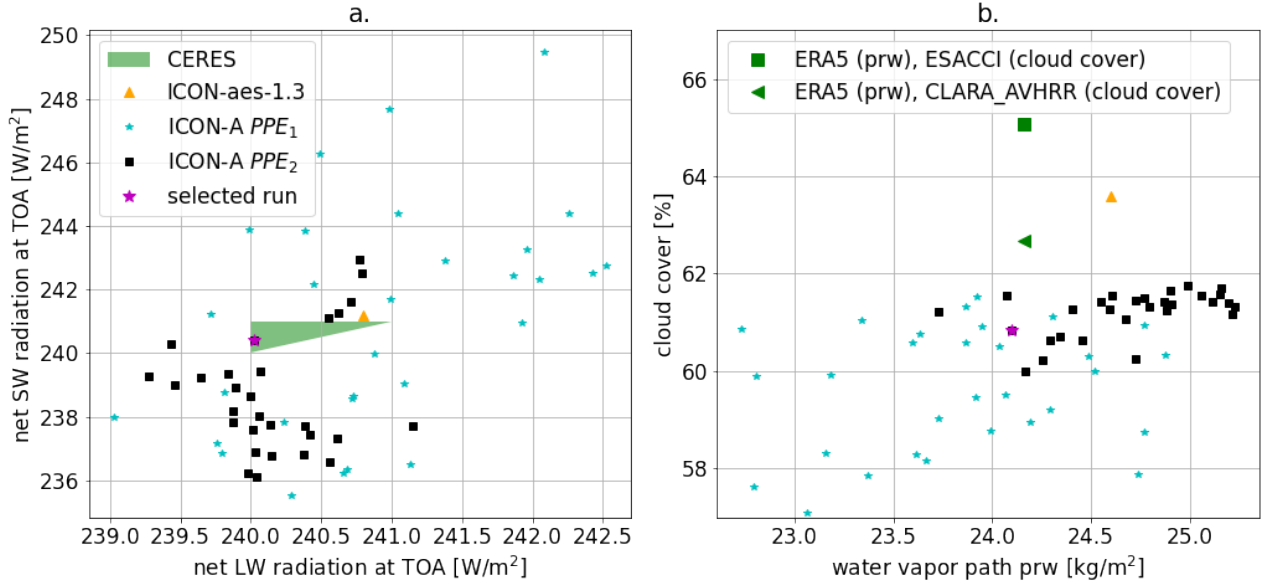
Figure 2. Physics output variables for PPE_1 (blue stars) and PPE_2 (black squares) compared to ICON-aes-1.3 (orange triangle) and observational datasets (green). Signs of convergence of history matching are visible already after one iteration (the distribution of the members of PPE_2 is slightly shifted towards higher cloud cover values and narrower). The magenta star marks the best performing configuration from PPE_2 (see right column of Table 5), used in the generation of the subsequent PPEs.

two PPEs (Fig. 3). However, Fig. 2 panel (b) shows that global cloud cover still remains lower than the observational data (of approximately 1% compared to CLARA-AVHRR, and 3% compared to ESACCI), despite PPE_2 yielding a slightly higher

285   cloud cover (closer to the observed range) than PPE_1. In Fig. 2, the magenta star marks the selected best performing model configuration in PPE_2. Following Giorgetta et al. (2018), our criterion for evaluating the model performance prioritizes the global radiation metrics, in particular the net TOA radiation budget, over cloud cover and water vapor path. The selected run is the only one falling within the observational range for both radiation metrics (green triangle in panel (a)).

     ICON-aes-1.3 exhibits a higher value of global cloud cover (orange triangle in Fig. 2.b) than our PPE_1 and PPE_2. The

290   resolutions of ICON-aes-1.3 (approximately 160 km) is coarser than PPE_1 and PPE_2 (approximately 80 km). The authors of (Giorgetta et al., 2018) have investigated the six tuning parameters used in $\mathcal{P}_{p1}$. Here, with these six parameters, we are not able to reach a similar performance for the cloud cover metric. This supports the fact that one should repeat the tuning process when the model resolution is changed (Crueger et al., 2018). Moreover, in addition to the parameters in $\mathcal{P}_{p1}$, the authors of (Giorgetta et al., 2018) explored other tuning parameters, and these results were not published because having a

295   negligible influence on their tuning process (as explained in their Section 5). In the next generation of PPEs (the second phase of our sequential approach), we investigate the impact of some of these parameters. Therefore, the parameter set $\mathcal{P}_{p2}$ contains parameters potentially having a stronger effect on cloud cover at the present resolution.
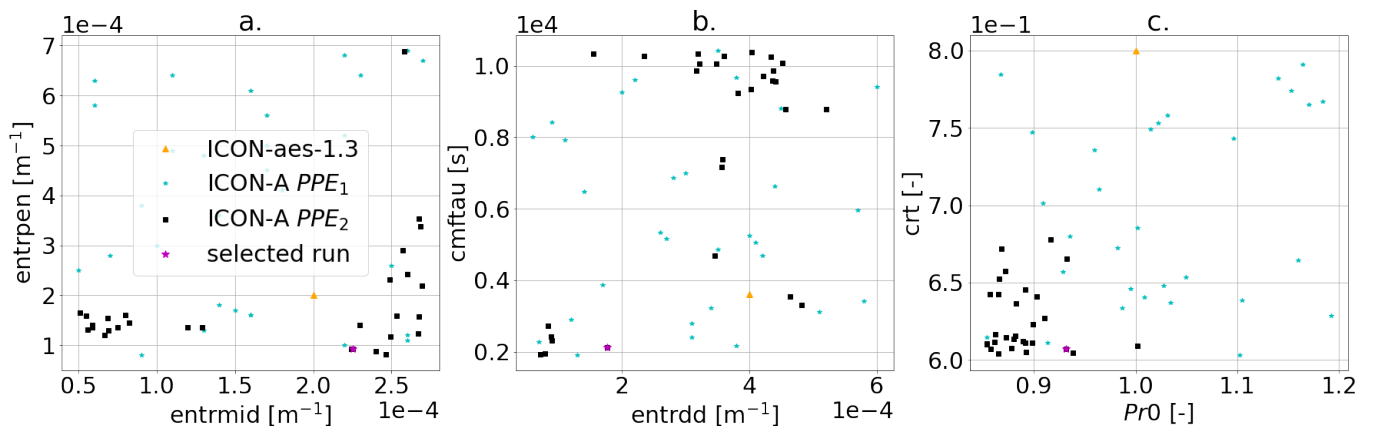
Figure 3. Sampled parameter values for PPE_1 (blue stars) and PPE_2 (black squares) compared to ICON-aes-1.3 (orange triangle). For each panel, two parameters are plotted on the two axes (see Table 3). Signs of convergence of history matching are visible already after one iteration (in the distribution of the members of PPE_2 being slightly shifted and narrower). The magenta star marks the best performing configuration from PPE_2 (see also right column of Table 5 for values), used in the generation of the subsequent PPEs.

Parameter set $\mathcal{P}_{p2}$ is used to generate PPE_3 with LHC sampling. A GP emulator is then trained on the outputs of PPE_3. The constructed GP emulator in this case also has a good predictive performance (measured by an average R^2 score of 0.75, as discussed in more details in Section 3.2.1 below), and we therefore use it for performing history matching and generating PPE_4. Also in this case history matching is shrinking the space of promising parameter configurations and the related output distribution. This can be seen in Fig. 4, where we show the distribution of the radiation metrics (in panel (a)), and the of global cloud cover versus water vapor path (in panel (b)) for both PPE_3 and PPE_4 (we refer the reader to Appendix C for plots of the related parameter distributions). While the new parameter set $\mathcal{P}_{p2}$ allows us to reach a global cloud cover consistent with observations, we also see that the spread of the PPE outputs is more than doubled compared to that of the previous PPEs (see yellow shaded rectangles in Fig. 4 showing the extent of Fig. 2). This increased spread also potentially increases the number of history matching iterations to converge towards the observational references. Given the high computational costs of generating these PPEs, we therefore use the best performing model configuration sampled so far, which belongs to PPE_2.

3.2.1 Performance of the GP emulator

We now analyze the performance of the GP emulator for the physics outputs considered. We refer the reader to Appendix B for details on Gaussian processes and the choice of the underlying hyperparameters. In Table 6, we show the average performance (R^2 score) of the GP emulators trained on the PPEs used for the tuning of the physics parameters (corresponding to PPE_1, PPE_2, PPE_3, PPE_4). The value reported in Table 6 is the average R^2 over all the five physics output metrics (defined in Table 1), and is computed using a 5-fold cross validation (https://scikit-learn.org/stable/). From these values, we conclude that the constructed emulators are indeed able to approximate the ICON-A physics outputs, which is also reflected in the fact that
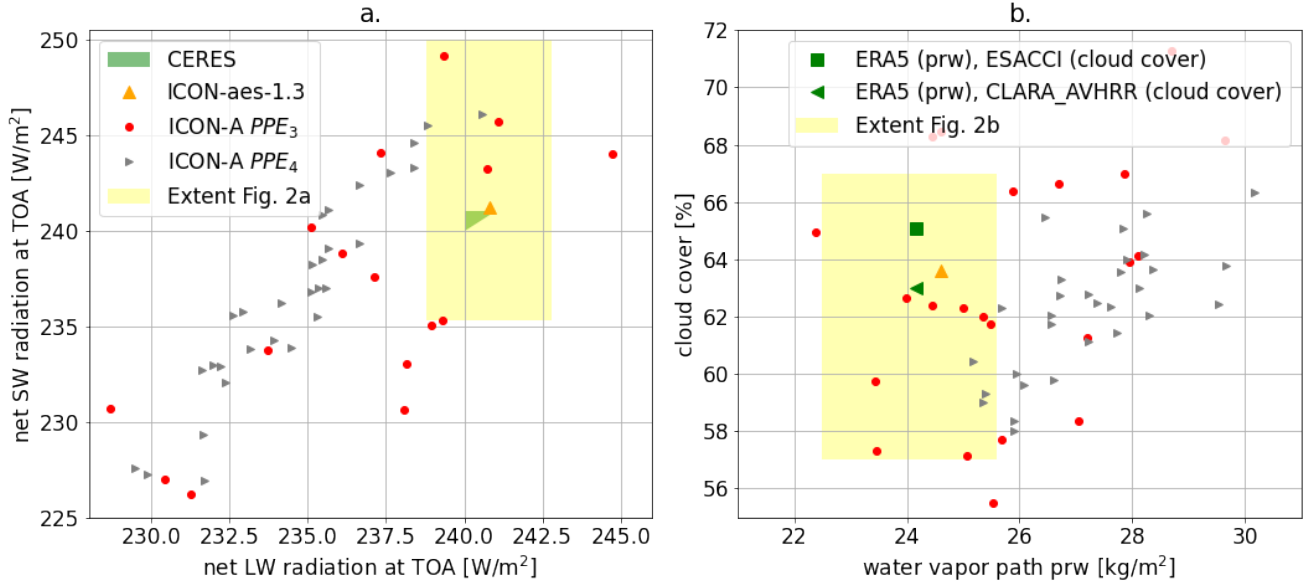
Figure 4. Physics output variables for PPE_3 (red circles) and PPE_4 (grey triangles) compared to ICON-aes-1.3 (orange triangle) and observational datasets. Also here, signs of convergence of the outputs to their observational values can be seen (in the distribution of the members of PPE_4 being slightly shifted and narrower).

PPE used for training	GP-emulator R^2-score
PPE_1	0.82
$PPE_1 + PPE_2$	0.79
PPE_3	0.75
$PPE_3 + PPE_4$	0.81

Table 6. Performance of the GP-emulator on PPE_1 to PPE_4. The R^2 value reported here is the average R^2 of the emulators for all physics variables (see Table 1). For each emulator, the R^2 is calculated via 5-fold cross validation on the training set (PPE points).

history matching shows signs of convergence already after the first iteration, as shown in the previous section. The number of PPE samples required for the GP regression to achieve the reported R^2 score is shown in Fig. 5.

3.2.2 Sensitivity analysis for the physics parameters and outputs

In this section we show the sensitivity analysis for the physics parameters and outputs, which supports our selection of parameters in the subsequent steps of our sequential approach, presented in Section 3.1. The analysis presented here is based on the calculation of Sobol indices, which in turn are calculated using the emulator constructed in the previous section. Generally
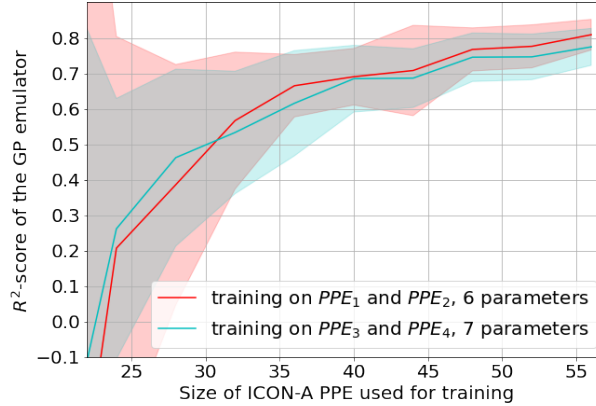
Figure 5. Average R^2 score of the physics outputs emulators, as a function of the size N of PPE used for training. For each N tested, fifty randomly drawn samples of size N were drawn from the entire set of ICON PPEs of size 60. The R^2 score is calculated for each size-N sample, and the mean (solid lines) and standard deviation (shaded areas) are estimated from these scores on the fifty samples. The red curve shows the R^2 for emulators trained on PPE_1 and PPE_2, the blue curve the R^2 for emulators trained on PPE_3 and PPE_4.

speaking, Sobol indices quantify the impact of one specific feature (tuning parameter, in our case) on the overall variance of the model output (the output metrics, in our case). Specifically, we focus on the first order Sobol index and on the total Sobol index. Given an emulator Y_{emul} for metric Y, the first order and total Sobol indices for the i-th parameter x_i are defined as

325 follows (Saltelli et al., 2010):

$$S_{1,(i,Y)} = \tfrac{1}{\text{Var}_{\boldsymbol{x}}(Y_{\text{emul}})} \, \text{Var}_{x_i}\big(\mathbb{E}_{\boldsymbol{x}\sim i}(Y_{\text{emul}} \,|\, x_i)\big) \, , \tag{6}$$

$$S_{\text{tot},(i,Y)} = \tfrac{1}{\text{Var}_{\boldsymbol{x}}(Y_{\text{emul}})} \, \mathbb{E}_{\boldsymbol{x}\sim i}\big(\text{Var}_{x_i}(Y_{\text{emul}} \,|\, \boldsymbol{x}_{\sim i})\big) \, , \tag{7}$$

where $\text{Var}_{\boldsymbol{x}}(Y_{\text{emul}})$ denotes the sample variance of the emulator over the distribution of all parameters $\boldsymbol{x}$, $\text{Var}_{x_i}(\cdot)$ the sample variance of the emulator over the distribution of parameter x_i, $\mathbb{E}_{\boldsymbol{x}\sim i}$ the expected value over all parameters but x_i, and $Y_{\text{emul}} \,|\, x_i$

330 denotes the emulator function with input parameter x_i kept fixed. The first order Sobol index $S_{1,(i,Y)}$ corresponds to the effect of varying x_i alone, averaged over all other inputs (parameters) variations, while $S_{\text{tot},(i,Y)}$ measures the total effect of varying x_i, which includes the variance coming from interactions of x_i with other parameters. In Figure 6 we show the $S_{1,(i,Y)}$ (on the x axis) and $S_{\text{tot},(i,Y)}$ (on the y axis) for the physics parameters and outputs. We use the GP emulator trained on PPE_1 for panels (a) to (e), and the one trained on PPE_3 for panels (f) to (j). The higher the values of the first and total Sobol indices for

335 a parameter and corresponding output, the higher the influence of that parameter on that output. Looking at panels (d) and (e) we see that the two most influential parameters in $\mathcal{P}_{\text{p1}}$ on cloud cover and water vapour metrics are crt and pr0, which are the ones we keep among the tuning parameters in $\mathcal{P}_{\text{p2}}$. In panels from (f) to (j), obtained from the emulator trained on PPE_3, we see that cvtfall has overall a large effect on all physics metrics, and the largest on cloud cover, while crt has the largest effect on the TOA net radiative budget, and we therefore decide to keep these tuning parameters in $\mathcal{P}_{\text{pd}}$ for PPE_5.
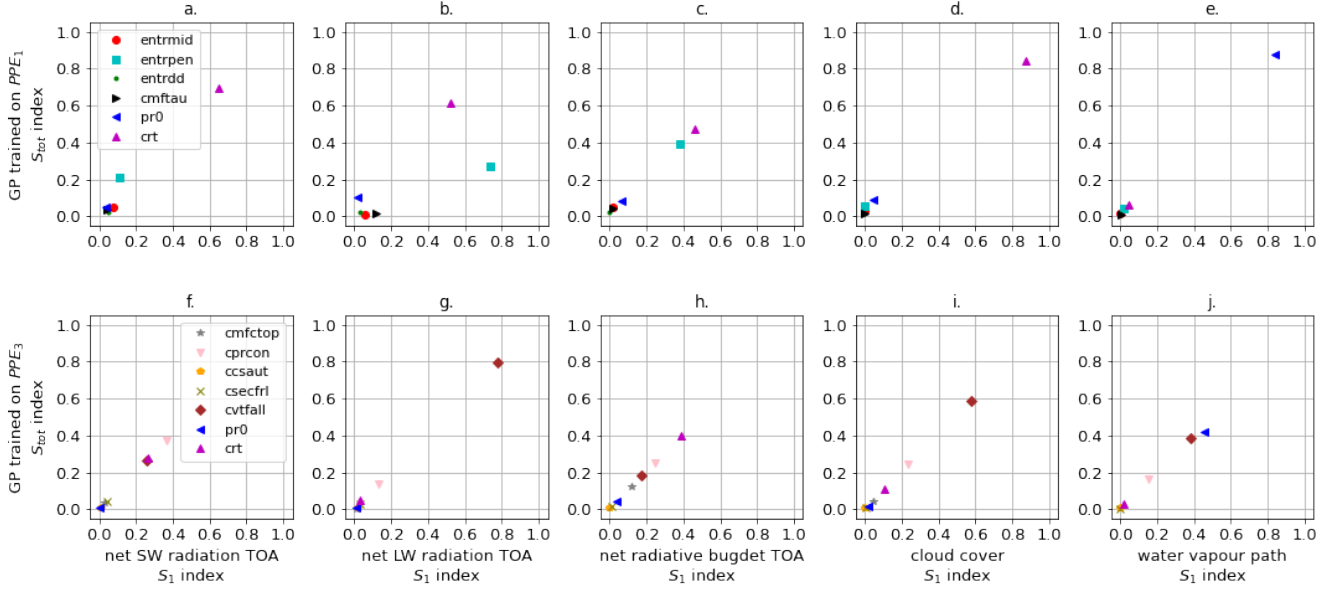
Figure 6. First order Sobol index S_1 (x-axis) and total Sobol index S_{tot} (y-axis) for the physics parameters (in legend) and outputs, net SW radiation at TOA (panels (a) and (f)), net LW radiation at TOA (panels (b) and (g)), net radiative bugdet at TOA (panels (c) and (h)), cloud cover (panels (d) and (i)), water vapour path (panels (e) and (j)). We use the GP trained on PPE_1 for panels (a) to (e) and trained on PPE_3 for panels (f) to (j). To calculate the Sobol indices, the sampling method of Saltelli et al. (2010) was used, with 70000 samples, allowing a converged value of the indices.

340

3.2.3 Visualization of the parameter-to-output maps

The previously trained emulator can also be used for the visualization of the parameter-to-output dependencies. These visualizations complement the sensitivity analysis presented in the previous section, and further helped us in the selection of the

345   tuning parameters to be kept across the phases of our sequential tuning approach. Generally, such visualizations are very useful for informing the user of the effect of a parameter on the outputs: they can help selecting the most influential parameters and the corresponding plausible ranges, potentially reducing the computational costs of tuning exercises.

Here we construct these parameter-to-output maps, similarly to what has been done by Mauritsen et al. (2012), with the important difference that the use of GP emulators in our case allows for a more extensive, or denser, exploration of the selected

350   parameter space. We exemplify such visualizations in Fig. 7, constructed from GP emulators for physics outputs trained on

PPE$_1$ and PPE$_2$ in the first two lines (Fig. 7 a-h) and on PPE$_3$ and PPE$_4$ in the last two lines (Fig. 7 i-p). The parameters that are not being changed are kept fixed to their best performing value from PPE$_2$ (marked with the magenta star in Figures 2 and 3 — although we emphasize that with the trained emulators one can very quickly generate new maps for different parameters). The red shaded areas in each plot denote the allowed output ranges from the observational data. For the parameters from $\mathcal{P}_{\text{p1}}$

355   varied, the value of global cloud cover (second row of Fig. 7) remains below the lower bound given by the observational data (at 62.7%), which is consistent with our observations in Fig. 2. This is the reason why we selected an increased parameter set $\mathcal{P}_{\text{p2}}$ for the next PPEs, which indeed had a higher influence on the global cloud cover (forth row of Fig. 7). We refer the reader to Appendix E for the parameter-to-output map constructed from PPE$_1$ and PPE$_2$ and showing the effect of the six parameters in $\mathcal{P}_{\text{p1}}$ on all physics metrics (Fig. E1). Likewise, the parameter-to-output map constructed from PPE$_3$ and PPE$_4$

360   and showing the effect of all parameters in $\mathcal{P}_{\text{p2}}$ is shown in Fig. E1.

Together with the previous Section 3.2.2, these maps allow us to identify which parameters are likely to be the most influential for our physics tuning metrics. The parameters that we identified as most influential for the physics output metrics are the critical relative humidity in the upper troposphere (crt) and the coefficient conversion from cloud water to rain (cprcon), influencing the radiation metrics and global cloud cover, together with the coefficient of sedimentation velocity of cloud ice

365   (cvtfall). These parameters have a strong linear influence (crt in Fig. 7 d. and h.) and non-linear influence (cprcon and cvtfall in Fig. 7 j., n., and l., p., respectively) on the physics metrics. Note that parameters governing cloud microphysical processes (e.g. fall velocities such as cvtfall) were identified as tuning parameters widely shared among climate models in Hourdin et al. (2017) synthesis paper (see Table ES4 therein).

3.3 Tuning of the dynamics outputs

370   We now discuss the simultaneous tuning of the physics and dynamics outputs. Due to the expected large variability of dynamics outputs (see next Section 3.3.1) which can potentially hinder the training of regression models, we expect history matching to require a large number of iterations and costly ICON simulations. Therefore, we adopt a similar approach to Giorgetta et al. (2018), in that we generate a PPE (PPE$_5$) and select the best performing model configurations. Also in this case, our criterion for evaluating the model performance gives a higher importance to the global radiation metrics, which are our primary tuning

375   goals, and puts less stringent requirements on the other tuning metrics.

The ML-based tuning of the physics output metrics discussed in the previous section serves as a basis for the second tuning step addressing the dynamics outputs. PPE$_5$ is generated by simultaneously varying the parameters in the set $\mathcal{P}_{\text{pd}}$ (with LHC sampling), while keeping the other parameters fixed to their best configuration obtained with history matching, from PPE$_2$ (see Table 5 and the magenta star in Fig. 2 and Fig. 3). The physics parameters in $\mathcal{P}_{\text{pd}}$ are selected based on a sensitivity

380   analysis with Sobol indices, as explained in Section 3.2.2. The choice of the dynamics parameters follows Giorgetta et al. (2018), with gkdrag and gkwake chosen for tuning the zonal wind stresses on the ocean surface, and rmscon affecting the zonal mean winds. In Fig. 8 we show the physics (panels (a) and (b)) and the dynamics (panels (c) and (d)) outputs from PPE$_5$, and highlight the two model configurations (the cyan and the red dot) which achieve the best model performance within PPE$_5$. The selected configurations are those closest to the observational range in panel (a) of Fig. 8, given that achieving a balanced
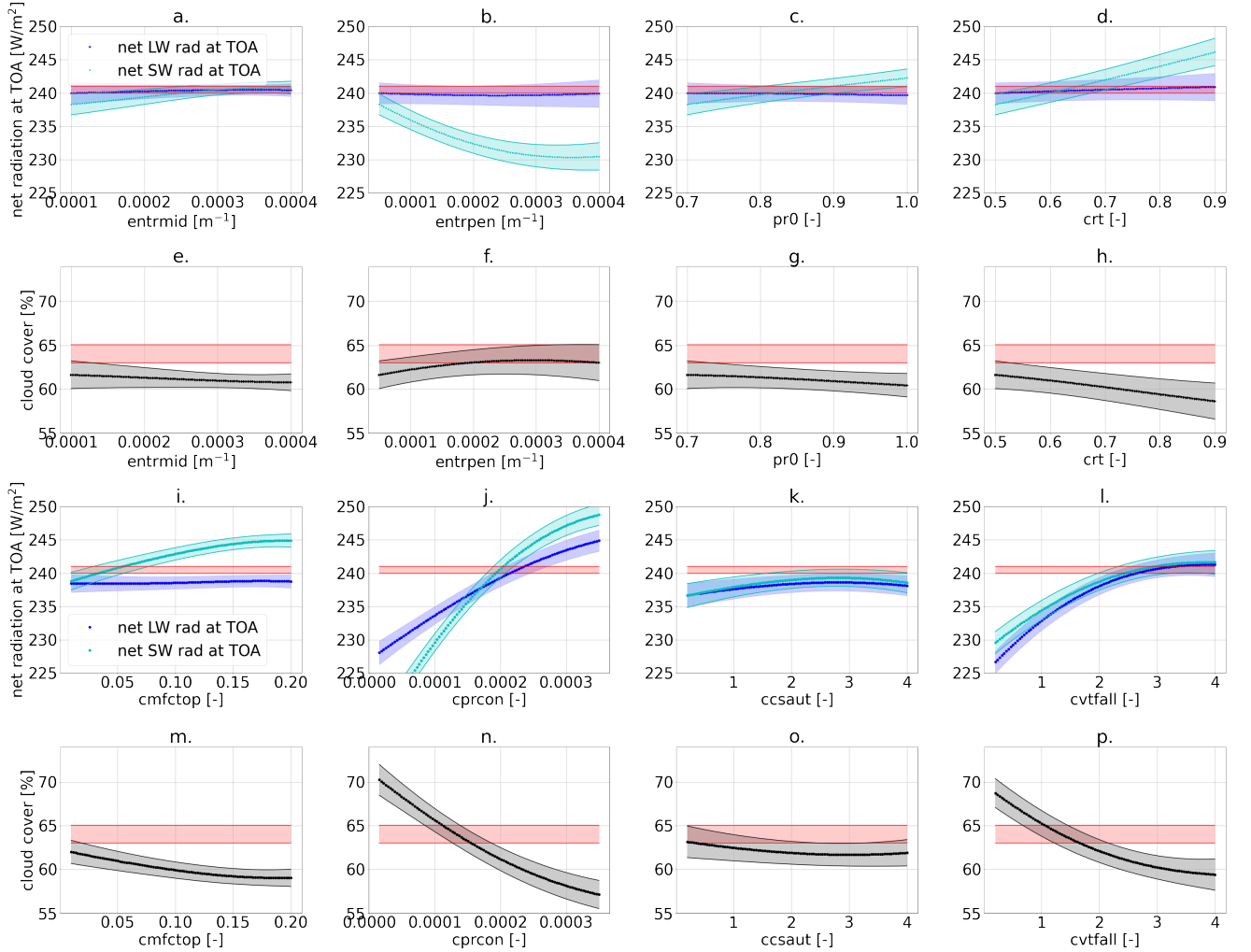
Figure 7. Parameter-to-output maps predicted with GP-emulators trained on PPE_1 and PPE_2 (a-h) and GP-emulators trained on PPE_3 and PPE_4 (i-p). In the first and third row (a-d and i-l) the net SW and LW radiation at the TOA are shown. In the second and forth row (e-h and m-p) the global cloud cover is shown. Figures a. and e. show the effect of entrmid, b. and f. that of entrpen, c. and g. of pr0, d. and h. of crt, i. and m. of cmfctop, j. and n. of cprcon, k. and o. of ccsaut, and l. and p. of cvtfall.

TOA radiation has a higher importance in our tuning experiment (Giorgetta et al., 2018). The values of the parameters for these two selected simulations are given in Table 7. These also achieve results comparable with the tuned ICON-aes-1.3, with the TOA radiation balance within the interval $[0,1]$ W/m^2, the TOA long- and short-wave radiation metrics within 1 W/m^2 from the observational range. Also for the other two physics output metrics the performance of the two selected configurations is comparable to ICON-aes-1.3, as they show less than 1% difference in global cloud cover compared to the observational range, and less than 0.5 kg/m^2 difference in the water vapor path. The differences with respect to reference data and ICON-aes-1.3

become more apparent when looking at the dynamics metrics. In panel (c) and (d) it can indeed be seen that the values of these metrics from the reference dataset are not covered by the generated PPE. For most of the metrics the differences of the selected configurations from the reference dataset remain comparable to those of ICON-aes-1.3, except for the mean zonal wind stress over the Southern Ocean (tauu SOO - see panel (c)), where the difference increased from roughly 0.005 N/m^2 to roughly 0.02 N/m^2. The values of the parameters for these two selected runs are given in Table 7. Given the different settings used in the manual tuning for ICON-aes-1.3 (160 km instead of the 80 km resolution used here, and the different time steps used), the differences in the optimal model configurations are not surprising. For instance, the model resolution strongly affects the parameters describing the unresolved orography, and thus the values of the corresponding parameters (Giorgetta et al., 2018).

In the next section we analyze the variability of the dynamics outputs, and we identify in it a possible explanation for the difficulty of matching them in our tuning. Afterwards, in Section 4, we evaluate the results from PPE$_5$ on model outputs not targeted during the tuning experiment, for a better assessment of the results and a better comparison with the previously tuned ICON-aes-1.3.

Physics Parameters	1st selected run	2nd selected run	Giorgetta et al. (2018)
entrmid	2.8526e-4	2.6751e-4	2e-4
entrpen	9.2951e-5	9.2951e-5	2e-4
entrdd	1.7662e-4	1.7662e-4	4e-4
cmftau	2114.6	2114.6	3600
pr0	0.93168	0.93168	1
crt	0.81681	0.80417	0.8
cmfctop	default value: 0.1	default value: 0.1	
cprcon	default value: 2.5e-4	default value: 2.5e-4	
ccsaut	default value: 2.0	default value: 2.0	
csecfrl	default value: 1.5e-5	default value: 1.5e-5	
cvtfall	1.7479	2.00239	
crs	0.88400	0.80222	
csatsc	0.8700	0.64369	
Dynamics Parameters			
gkdrag	0.17404	0.20595	0.1
gkwake	0.08262	0.087592	0.01
rmscon	0.91864	0.82209	0.87
gpicmea	28.375	53.976	
gstd	8.40780	13.025	

Table 7. Values of the parameters for the two members of PPE$_5$ yielding the best output metrics, shown as cyan square and red triangle in Fig. 8. For comparison, the values of the parameters tuned by Giorgetta et al. (2018) are given as well.
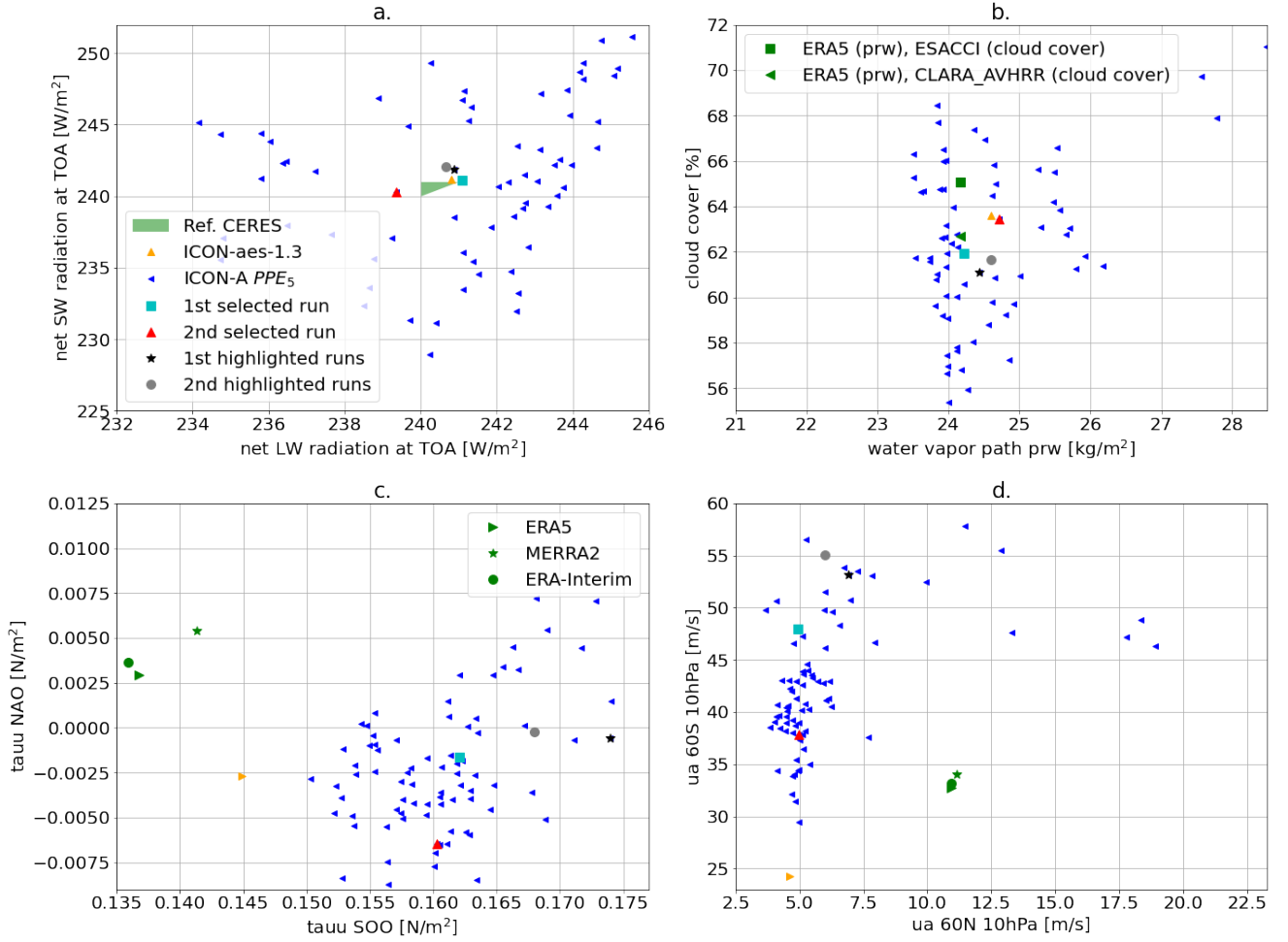
Figure 8. Physics (top row) and dynamics (bottom row) output variables for PPE_5 (blue triangles), compared to ICON-aes-1.3 (orange triangle) and observational datasets. Two selected PPE members corresponding to the best performing configurations are highlighted (cyan square and red triangle). For comparison, two other runs are also highlighted (black circles).

3.3.1 Analysis of output variability

We now use PPE_5 to analyze the internal variability of the investigated output metrics and compare them to the parameters' effects. The year-to-year variability of the output metrics is shown in Fig. 9 where we plot the long- vs. short-time averages of the considered outputs, for 30 runs of PPE_5. Additional data complementing the information of Fig. 9 can be found in Appendix D. In Fig. 9 it can be clearly seen that the dynamics outputs (panels in the lower row) have a larger variability across years compared to the physics ones (upper row), which is apparent from the larger spread around the diagonal (no spread would signify no variance), and the larger error bar (which represents the standard deviation over the yearly averages). In each panel

410 we also report the ratio between the mean spread across years S_{yrs} and the PPE spread S_{PPE}, which for each output metric Y are defined as:

$$S_{\text{yrs}} = \sqrt{\frac{1}{n} \sum_{i=1}^{n} \text{Var}_{\text{years,i}}(Y)} \, , \tag{8}$$

$$S_{\text{PPE}} = \sqrt{\frac{1}{n} \sum_{i=1}^{n} \left(Y_i - \overline{Y} \right)^2} \, , \tag{9}$$

where n denotes the size of the PPE, $\text{Var}_{\text{years},i}(Y)$ the variance of output Y over the simulated years for the i-th PPE member,

415 Y_i the ten-year mean of output Y for the i-th PPE member, and $\overline{Y}$ the average of the Y_i over all PPE members. The ratio $S_{\text{years}}/S_{\text{PPE}}$ gives a quantitative measure of the comparison between the yearly output variability and the effects of changing parameters in the PPE. It is clear that for the dynamics outputs, especially the zonal wind stresses on the ocean surface, this ratio is almost one order of magnitude larger than for the physics ones.

An additional source of uncertainty in the dynamics output metrics is their restricted geographical location, which exposes

420 them to biases in spatial patterns. The low variability in the physics variables, which are global means, is consistent with the common observation that already simulations as short as one year can give good tuning results, though using more years, as for instance a full decade used in (Giorgetta et al., 2018), has the benefit to include a larger variation of prescribed boundary conditions as for example El Niño, La Niña or neutral years.

The analysis shown in Fig. 9 shows that for dynamics outputs, the internal variability is almost of the same order of magnitude

425 of the PPE variance, and can therefore partly hide the effects of changing parameters, as discussed above.

4 Evaluation of the selected runs

Now we test our selected model configurations on different variables that were not targeted during the tuning. We call these "evaluation metrics". Specifically, we assess whether the outputs of our selected parameter configurations are also compatible with the evaluation metrics, i.e., within the spread of the reanalysis and observational datasets used as reference. This evaluation

430 step allows us to check whether the tuning process has induced significant biases on metrics not targeted during the tuning (i.e., overtuning to the target metrics). The evaluation metrics that we inspect are the global multi-annual averages (from 1980 to 1989 included) of the surface temperature (ts), the total precipitation (pr), the pressure at sea level (psl), the vertically integrated cloud ice (clivi), and the vertically integrated cloud condensed water content (clwvi). The results of this evaluation step are shown in Fig. 10. For most of the computed evaluation metrics, our selected model configurations are within the observational

435 range given by the spread of the reanalysis and observational datasets used as reference (green symbols and lines in Fig. 10), thus indicating that our tuning experiment had a beneficial effect on the evaluation metrics that were not targeted by the tuning. This is the case for the two selected runs and the two highlighted runs from the ICON-A PPE_5. These selected model configurations show a slight positive bias $< 0.1°\text{C}$ on the global average of the surface temperature compare to the reference values. We conclude that our tuning experiment successfully produced configurations largely comparable to ICON-aes-1.3.

440 While it did not show substantial improvement over the manually tuned version, which is difficult to improve upon, we discuss the limitations of our approach and propose potential improvements in the next section.
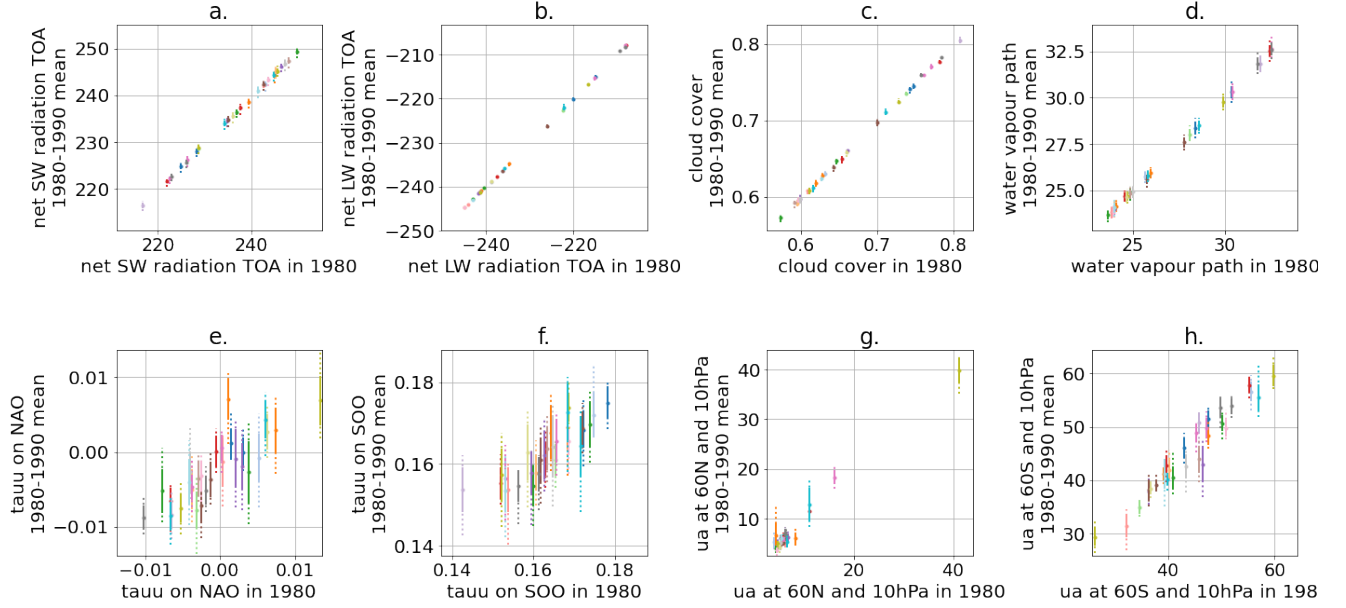
Figure 9. Ten-year mean (1980-1989, y axis) against the mean of one particular year (here 1980, x axis), for the physics (top row, panels (a) to (d)) and dynamics (bottom row, panels (e) to (h)) output variables for 30 runs of PPE_5, represented by different colors. For each data point, the dotted vertical line shows the spread of the annual mean across the ten years (maximum and minimum values), and the solid vertical line denotes one standard deviation, calculated on the 1980-1989 period.
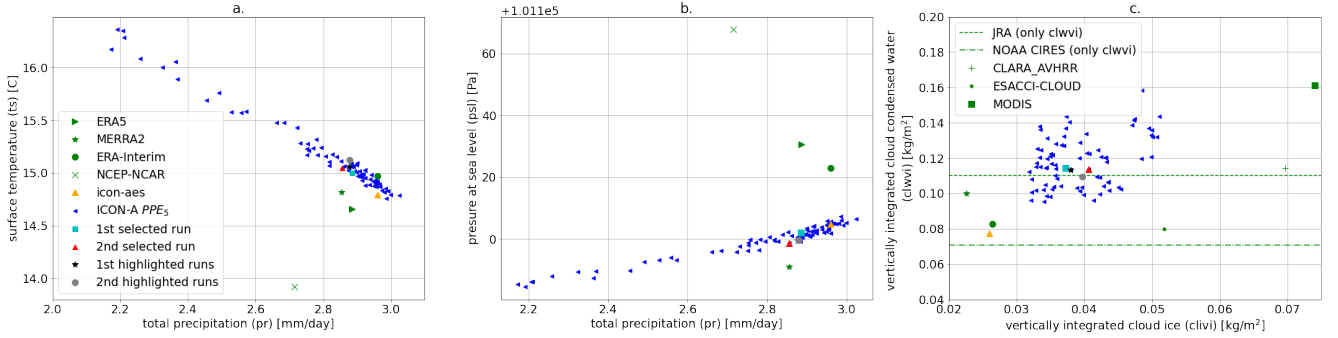
Figure 10. Five evaluation metrics averaged on the 1980-1989 (included) period for the PPE_5 (blue, cyan, red, black, gray), the ICON-aes-1.3 (orange triangle), and reanalysis datasets and observational datasets (green). For the datasets starting after 1980, the time period considered is the earliest available 10 years: for CLARA (AVHRR) and ESACCI CLOUD (AVHRR-fv3.0) it is 1982-1991, for MODIS it is 2002-2011.

5   Discussions and Conclusions

In this work, we develop an ML-based tuning approach and apply it to the atmospheric component of the ICON climate model (ICON-A). Our approach is inspired by history matching (Williamson et al., 2013, 2017), which balances an extensive exploration of the tuning parameter space with the need of minimizing the number of required ICON-A model simulations. This exploration is aided by building and using emulators, here Gaussian processes (GPs), for each of the considered output metrics. The emulator approximates the climate model simulation outputs for arbitrary values of the tuning parameters, and can be used to create large emulated metrics ensembles at a much cheaper computational cost. We integrate a history-matching-inspired method in a sequential approach, where at each phase different parameter sets are sequentially constrained. We first apply our approach to the tuning of physics output metrics (globally averaged radiation and cloud properties), and in a second step we tune also for dynamics output metrics (related to geographically specific atmospheric circulation properties) using a PPE consisting of 80 ten-year ICON-A runs. The ML-based tuning of physics parameterizations, with just one iteration and a total of 60 model simulations, is already sufficient to achieve a model configuration yielding a global TOA net radiation budget in the range of $[0, 1]$ W/m^2, global radiation metrics and water vapor path consistent with the reference observations, and a globally averaged cloud cover differing by only 2% with respect to the observations. Note that these results, in particular the number of iterations necessary to converge to the observational range, generally depend on the specific setup. Furthermore, we remark that our approach presents some differences to traditional history matching implementations. While it allowed us to draw some configurations with outputs compatible with observations for some metrics, a thorough characterization of the space of plausible parameters (the not-ruled-out-yet space (Williamson et al., 2013)) is beyond the scope of our work, and would require several iterations of standard history matching.

In the simultaneous PPE-based tuning of physics and dynamics parameterizations, we achieve a TOA radiation balance within the interval $[0, 1]$ W/m^2, TOA long- and short-wave radiation metrics to within 1 W/m^2 from the targeted range, but are not able to reduce the biases in the dynamics output metrics with respect to the previously manually tuned ICON-aes-1.3. The PPE for this tuning step allows us to perform an analysis of the physics and dynamics outputs variability and its comparison with the parameters' effects. This analysis reveals a larger year-to-year variability of the dynamics compared to the physics output metrics. This, combined with the sensitivity of the dynamics metrics to geographic pattern, highlights potential limitations that emulator-based approaches may face when tuning for these dynamics metrics. This suggests at the same time that metrics averaged over broader spatial regions may suffer less from these issues and be more amenable to emulator-based approaches, although too much averaging in space would make the tuning target less characteristic. For the case of the dynamics variable which are proxies for polar stratospheric vortices (zonal mean zonal wind, averaged at 60° North and 60° South, at 10 hPa, 10-year average), a possible way to reduce the noise would be to increase the simulation duration and to average the field over only winter or summer months. A further evaluation of the selected model configurations on metrics that were not targeted during tuning suggests that our approach does not cause overtuning to the tuning targets, and for our use case results in a model configuration that can be considered of a similar performance as the previously tuned ICON-aes-1.3.

475 Our sequential approach, where at each phase only a small subset of parameters is varied, allows to keep the costs of the PPEs relatively low (with 30 members we could reach good emulator accuracies), and to obtain ICON-A model configurations showing an overall performance comparable to ICON-aes-1.3 on most of the selected tuning metrics. However, such an approach may face the problem of neglecting some of the (non-linear) parameter interdependencies and the possible feedbacks. In situations where such parameter interactions and their hierarchy of importance are largely unknown, we would recommend

480 simultaneously tuning all parameters, when computationally feasible. Indeed, while with our analysis we are able to identify which parameters are influential for the chosen metrics (see Section 3.2.3), we cannot establish a clear hierarchy of which of these should be tuned in a sequential manner. This is exemplified by Figures 4 and 8, with the PPEs showing a large spread in the global radiative metrics despite some of the physics parameters being kept fixed. Furthermore, accounting for all parameter dependencies and feedbacks could be particularly important for tuning coupled models, e.g., for properly accounting for the

485 interactions between atmosphere and ocean. The number of parameters that can be tuned simultaneously is ultimately limited by the available computational resources, since the required size of the PPEs scales with the size of the tuning parameter space. Therefore, sensitivity analysis as presented here becomes a crucial tool to identify and keep only the most important parameters in each model component.

We also note that even though history matching is constructed to minimize the number of climate model simulations for the

490 PPEs, this number is still the major computational bottleneck in tuning, which gets worse when tuning models at resolutions higher than the one considered here. Again, including as much prior knowledge as possible in the choice of the parameters, which in a Bayesian setting amounts to the selection of a prior distribution for the optimal parameter values, will be important. Such knowledge of a prior distribution may for instance be obtained by the computationally cheaper tuning of the same model at lower resolutions, provided the same parameterization schemes are used. Incorporating such prior knowledge could reduce

495 the size of the PPEs and the number of history matching iterations required to converge to an optimal model configuration (Fletcher et al., 2022), compared to starting from general uninformative priors as we did here (with LHC sampling).

Finally, while here we explored the feasibility of ML-based tuning approaches to improve the tuning of climate models, the seamless integration of such methods within the specific climate modeling framework - to practically enable an automatic application - is an aspect that needs to be addressed in further studies. Some aspects of model tuning, such as the choice

500 of tuning metrics, will remain subjective, as highly dependent on the details and complexity of the model as well as on its intended uses. Other steps however, such as sensitivity analysis and selection of tuning parameters, their exploration and the evaluation of the outcomes could be incorporated, at least partly, in an automated approach. It is therefore important to understand which design choices are best suited for such automatic approaches, as we foresee that these will lead to more accurate and potentially computationally cheaper model tuning, also making this important step in climate model development

505 more objective and reproducible.

Code availability. The code is published under https://github.com/EyringMLClimateGroup/bonnet24gmd_automatic_tuning_atm. The software code for the ICON model is available from https://icon-model.org.
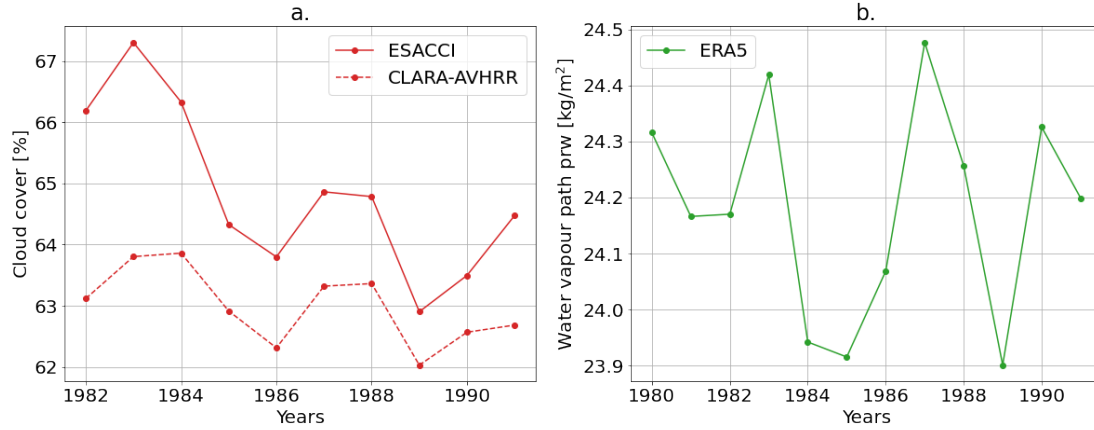
Figure A1. Time series of the observational products used for the cloud cover and the water vapour path

Appendix A: Times series of the observational products used

Figure A1 shows the time series of the observational products used for the cloud cover and the water vapour path. The ten
year period 1980-1989 was used for the tuning of the dynamic outputs of ICON-A. For the cloud cover observational datasets,
the earliest year available is 1982, therefore we added the years 1990-1991 in our tuning analysis. The variability in the years
illustrates the internal climate variability. We remark that other observational products exist for these outputs but do not include
the studied years. For example, ESACCI-WATERVAPOUR starts from year 2002, MODIS starts from year 2002, or Cloudsat
starts from year 2006.

Appendix B: Details on GP emulators and choice of the underlying hyperparameters

In this appendix we give a brief description of the Gaussian process (GP) regression framework used to construct emulators in
this work, and provide the relevant details regarding the hyperparameters used in their implementation. Gaussian processes are
widely used in the context of Bayesian optimization, as they are a method for describing distributions over unknown functions,
and can be efficiently updated, or trained, using samples from the ground-truth distribution (Rasmussen and Williams, 2005).
In our case, the function we want to approximate with GP regression is that describing the dependence of a specific output Y
of the climate model, on a set of tuning parameters $\boldsymbol{x}$, which we call $Y_{\mathrm{model}}(\boldsymbol{x})$. The output of a Gaussian process trained on
set $\mathcal{T} = \{\boldsymbol{x}_i, Y_{\mathrm{model}}(\boldsymbol{x}_i)\}_i$ of ground-truth samples (ICON-A model runs in our case) can be written as:

$$f(\boldsymbol{x})|\mathcal{T} \sim \mathcal{GP}(\mu(\cdot), C_{\cdot,\cdot}) , \tag{B1}$$

where $\mathcal{GP}$ denotes the GP function distribution with $\mu(\boldsymbol{x})$ and C respectively being the mean function and the covariance
matrix that implicitly depend on $\mathcal{T}$, i.e., have been updated with the knowledge of the training data $\mathcal{T}$ using Bayes' rule.

Closed form expressions for these functions are available and can be found in Rasmussen and Williams (2005). That is to say, given a new configuration $\boldsymbol{x}$ of tuning parameters, a GP trained on an ICON-A PPE for a given variable Y would output a normally distributed random variable with mean $\mu(\boldsymbol{x})$ and variance $\sigma^2(\boldsymbol{x})$ (which can also be explicitly calculated from the knowledge of the covariance matrix C (Rasmussen and Williams, 2005)). We therefore interpret $\mu(\boldsymbol{x})$ as our GP emulator prediction for Y, and $\sigma^2(\boldsymbol{x})$ as the associated uncertainty, and write:

$$Y_{\text{emul}}(\boldsymbol{x}) \equiv \mu(\boldsymbol{x}) , \tag{B2}$$

$$\text{Var}(Y_{\text{emul}}(\boldsymbol{x})) \equiv \sigma^2(\boldsymbol{x}) , \tag{B3}$$

which we use in Eq. (1) in the main text.

Importantly, the properties of the GP, in particular of the covariance matrix C, depend on the choice of a *kernel function* $k(\boldsymbol{x}, \boldsymbol{x}')$, which describes how the predictions at two points $\boldsymbol{x}$ and $\boldsymbol{x}'$ are correlated. Kernel functions may also contain trainable hyperparameters, which are typically optimized by maximizing the log marginal likelihood with respect to the training dataset (Rasmussen and Williams, 2005).

For our implementations we used the GP regression library implemented in scikit-learn package (https://scikit-learn.org/stable/). We found Matèrn kernels to yield the highest prediction accuracy (which we measure via R^2 coefficient). Matèrn kernels have two hyperparameters: a lengthscale l and a smoothness parameter ν. The length scale is typically the distance by which one can extrapolate outside the training data points: smaller values of l correspond to more rapidly varying functions that the GP can fit. This hyperparameter, together with the overall scale of the kernel, is optimized using the L-BFGS-B optimization (Jorge Nocedal, 2006) pre-implemented in scikit-learn. For the smoothness parameter ν, four values were tested: $\nu = 0.5$ corresponds to the absolute exponential kernel, $\nu = 1.5$ to a one-time differentiable function, $\nu = 2.5$ to a twice differentiable function and $\nu \to \infty$ to a radial basis function (RBF) kernel. These four values of ν allow a computational cost around ten times smaller than other values, since they do not require to evaluate the modified Bessel function (Rasmussen, 2006). The values of $\nu = 2.5$ and $\nu \to \infty$ yield large negative R^2-scores, so are not represented here. In panel (a) of Fig. B1 we observe a comparable performance of the GP emulator for $\nu = 0.5$ (absolute exponential kernel) and $\nu = 1.5$.

Other hyperparameters in the GP optimization are the noise level α (which can be interpreted as the variance of Gaussian noise added to the training data, with the aim of increasing the numerical stability of GP evaluations) and the number of random hyperparameter initializations for the log marginal likelihood optimization (denoted with n_restart). Several values of α between 10^{-15} and 10^{-5} were tested. We show these tests in panel (b) Fig. B1. The values of $\alpha < 10^{-10}$ yield large negative R^2 scores. A change of α for $10^{-10} < \alpha < 10^{-5}$ does not have a significant effect on the performance of the GP emulator. Finally, we also tested several values of the n_restart, between 0 and 100, as shown in panel (c) of Fig. B1. From the tests presented in Fig. B1, the following values of the three hyperparameters are chosen (which are also default values in scikit-learn): $\nu = 1.5$, $\alpha = 10^{-10}$ and n_restart$= 0$.
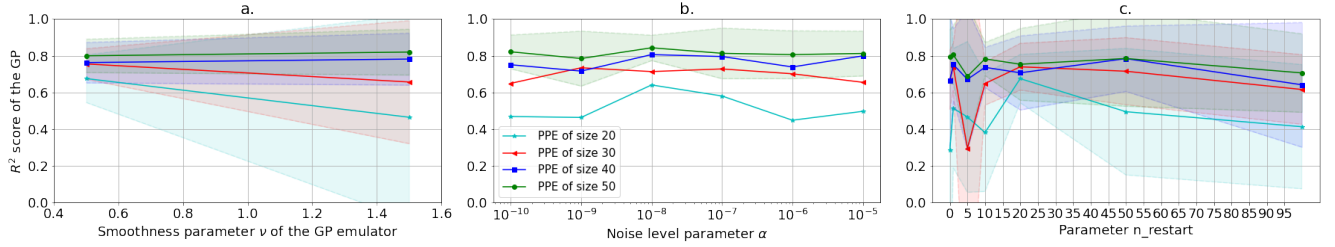
Figure B1. Performance (R^2 coefficient, calculated with 5-fold cross-validation) of the GP emulator with Matèrn kernel trained on PPE_1 and PPE_2, for different choices of hyperparameters: (a) for different values of ν, (b) for different values of α, and (c) for different values of n_restart.

Appendix C: Additional information on the generated PPEs

In this appendix we show additional data for the PPEs we generated in this work. Specifically, in Fig. C1 we show the sampled parameter values for PPE_3 (red circles) and PPE_4 (grey triangles), where signs of (slow) convergence of history matching are visible already after one iteration (in the distribution of the members of PPE_4 being slightly shifted and narrower). Figure C2 shows the sampled parameter values for PPE_5 (blue triangles), with the cyan square and red triangle marking the best performing configurations reported in Table 7 in the main text.

Appendix D: Times series of the physics and dynamic metrics

In this appendix we show additional information complementing Fig. 9 in Section 3.2.1 in the main text. In Fig. D1 we show the yearly averages of the physics (top row, panels (a) to (d)) and dynamics (bottom row, panels (e) to (h)) output variables for the 30 runs of PPE_5 corresponding to Fig. 9. Also in these time series the higher year-to-year variability of the dynamics outputs compared to the physics ones can be clearly seen.

Appendix E: Additional information on parameter-to-output maps

In this appendix we show additional information on the parameter-to-output maps discussed in Section 3.2.3. In Fig.E1 (resp. Fig. E2) we show the parameter-to-output map predicted with the GP-emulators trained on PPE_1 and PPE_2, (resp. PPE_3 and PPE_4), on parameter set $\mathcal{P}_{\text{p1}}$. (resp. $\mathcal{P}_{\text{p2}}$). In Fig. E2 o-u we can see that parameter set $\mathcal{P}_{\text{p2}}$ does indeed allow for a higher (and closer to the observational values) global cloud cover compared to $\mathcal{P}_{\text{p1}}$ (Fig. E1).
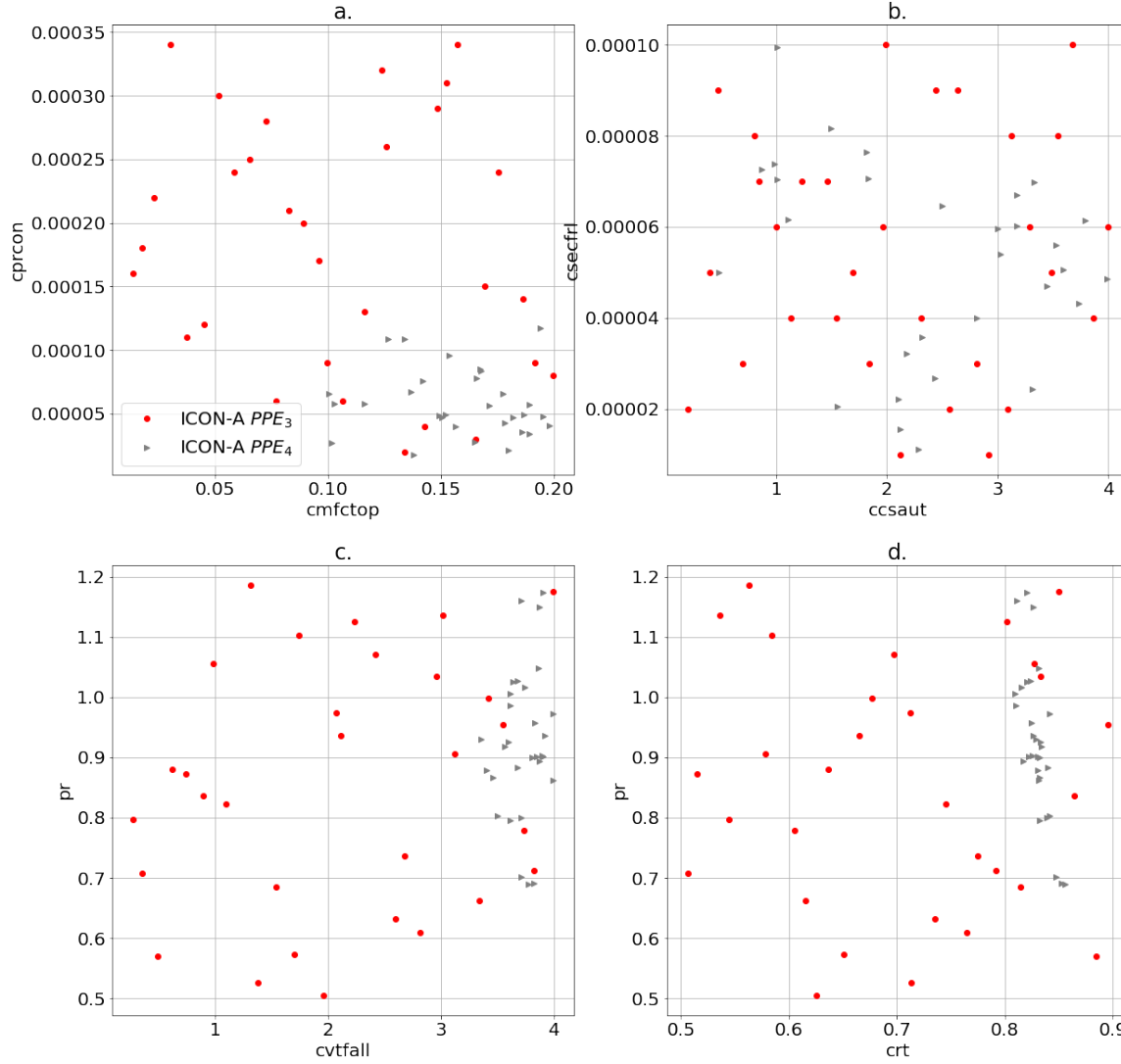
Figure C1. Sampled parameter values for PPE_3 (red circles) and PPE_4 (grey triangles). For each panel, two parameters are plotted on the two axes (see Table 3). The two PPEs are generated with parameter set $\mathcal{P}_{p2}$. Signs of (slow) convergence of history matching are visible already after one iteration (in the distribution of the members of PPE_4 being slightly shifted and narrower). The extents of the plots includes all the PPE_4, but not all of the PPE_3.

Author contributions. PB developed the ML-based tuning approach and performed the PPE simulations with ICON-A. She led the analysis with support of LP. VE formulated the research question and concept. All authors discussed the methodology and findings. LP and PB wrote the manuscript with contributions from all authors.

575

Competing interests. The authors declare no competing interests.

Acknowledgements. This study was funded by the European Research Council (ERC) Synergy Grant "Understanding and Modeling the Earth System with Machine Learning" (USMILE) under the Horizon 2020 Research and Innovation program (Grant Agreement No. 855187) and by the "Earth System Models for the Future (ESM2025)" project under the European Union's Horizon 2020 research and innovation program (Grant Agreement No. 101003536), and by the "Artificial Intelligence for Enhanced Representation of Processes and Extremes in Earth System Models" (AI4PEX) under the EU's Horizon Europe program (Grant agreement ID: 101137682). VE was additionally supported by the Deutsche Forschungsgemeinschaft (DFG, German Research Foundation) through the Gottfried Wilhelm Leibniz Prize awarded to Veronika Eyring (Reference No. EY 22/2-1). The contribution of LP and MS was made possible by the DLR Quantum Computing Initiative and the Federal Ministry for Economic Affairs and Climate Action; https://qci.dlr.de/projects/klim-qml. This work used resources of the Deutsches Klimarechenzentrum (DKRZ) granted by its Scientific Steering Committee (WLA) under project ID 1179 (USMILE) and 1083 (Climate Informatics). We acknowledge the provision for post-processing scripts and the advice provided by Renate Brokopf from Max Planck Institute for Meteorology. We would like to thank Dr. Axel Lauer for his valuable comments and suggestions to improve the manuscript. We would like to extend our sincere gratitude to the two reviewers Prof. Dr. Frédéric Hourdin and Dr. Qingyuan Yang, and editor Dr. Peter Caldwell, whose invaluable feedback and constructive comments significantly contributed to the improvement and quality of this work.

References

Baldwin, M. P., Ayarzagüena, B., Birner, T., Butchart, N., Butler, A. H., Charlton-Perez, A. J., Domeisen, D. I. V., Garfinkel, C. I., Garny, H., Gerber, E. P., Hegglin, M. I., Langematz, U., and Pedatella, N. M.: Sudden Stratospheric Warmings, Reviews of Geophysics, 59, https://doi.org/10.1029/2020rg000708, 2021.

595 Cleary, E., Garbuno-Inigo, A., Lan, S., Schneider, T., and Stuart, A. M.: Calibrate, emulate, sample, Journal of Computational Physics, 424, 109 716, https://doi.org/10.1016/j.jcp.2020.109716, 2021.

Couvreux, F., Hourdin, F., Williamson, D., Roehrig, R., Volodina, V., Villefranque, N., Rio, C., Audouin, O., Salter, J., Bazile, E., Brient, F., Favot, F., Honnert, R., Lefebvre, M.-P., Madeleine, J.-B., Rodier, Q., and Xu, W.: Process-Based Climate Model Development Harnessing Machine Learning: I. A Calibration Tool for Parameterization Improvement, Journal of Advances in Modeling Earth Systems, 13,
600 https://doi.org/10.1029/2020ms002217, 2021.

Crueger, T., Giorgetta, M. A., Brokopf, R., Esch, M., Fiedler, S., Hohenegger, C., Kornblueh, L., Mauritsen, T., Nam, C., Naumann, A. K., Peters, K., Rast, S., Roeckner, E., Sakradzija, M., Schmidt, H., Vial, J., Vogel, R., and Stevens, B.: ICON-A, The Atmosphere Component of the ICON Earth System Model: II. Model Evaluation, Journal of Advances in Modeling Earth Systems, 10, 1638–1662, https://doi.org/10.1029/2017ms001233, 2018.

605 Dee, D. P., Uppala, S. M., Simmons, A. J., Berrisford, P., Poli, P., Kobayashi, S., Andrae, U., Balmaseda, M. A., Balsamo, G., Bauer, P., Bechtold, P., Beljaars, A. C. M., van de Berg, L., Bidlot, J., Bormann, N., Delsol, C., Dragani, R., Fuentes, M., Geer, A. J., Haimberger, L., Healy, S. B., Hersbach, H., Hólm, E. V., Isaksen, L., Kållberg, P., Köhler, M., Matricardi, M., McNally, A. P., Monge-Sanz, B. M., Morcrette, J., Park, B., Peubey, C., de Rosnay, P., Tavolato, C., Thépaut, J., and Vitart, F.: The ERA-Interim reanalysis: configuration and performance of the data assimilation system, Quarterly Journal of the Royal Meteorological Society, 137, 553–597,
610 https://doi.org/10.1002/qj.828, 2011.

Domeisen, D. I., Butler, A. H., Charlton-Perez, A. J., Ayarzagüena, B., Baldwin, M. P., Dunn-Sigouin, E., Furtado, J. C., Garfinkel, C. I., Hitchcock, P., Karpechko, A. Y., Kim, H., Knight, J., Lang, A. L., Lim, E., Marshall, A., Roff, G., Schwartz, C., Simpson, I. R., Son, S., and Taguchi, M.: The Role of the Stratosphere in Subseasonal to Seasonal Prediction: 1. Predictability of the Stratosphere, Journal of Geophysical Research: Atmospheres, 125, https://doi.org/10.1029/2019jd030920, 2020a.

615 Domeisen, D. I. V., Butler, A. H., Charlton-Perez, A. J., Ayarzagüena, B., Baldwin, M. P., Dunn-Sigouin, E., Furtado, J. C., Garfinkel, C. I., Hitchcock, P., Karpechko, A. Y., Kim, H., Knight, J., Lang, A. L., Lim, E., Marshall, A., Roff, G., Schwartz, C., Simpson, I. R., Son, S., and Taguchi, M.: The Role of the Stratosphere in Subseasonal to Seasonal Prediction: 2. Predictability Arising From Stratosphere-Troposphere Coupling, Journal of Geophysical Research: Atmospheres, 125, https://doi.org/10.1029/2019jd030923, 2020b.

Dunbar, O. R. A., Garbuno-Inigo, A., Schneider, T., and Stuart, A. M.: Calibration and Uncertainty Quantification of Convective Parameters
620 in an Idealized GCM, Journal of Advances in Modeling Earth Systems, 13, https://doi.org/10.1029/2020ms002454, 2021.

Fletcher, C. G., McNally, W., Virgin, J. G., and King, F.: Toward Efficient Calibration of Higher-Resolution Earth System Models, Journal of Advances in Modeling Earth Systems, 14, https://doi.org/10.1029/2021ms002836, 2022.

Gelaro, R., McCarty, W., Suárez, M. J., Todling, R., Molod, A., Takacs, L., Randles, C. A., Darmenov, A., Bosilovich, M. G., Reichle, R., Wargan, K., Coy, L., Cullather, R., Draper, C., Akella, S., Buchard, V., Conaty, A., da Silva, A. M., Gu, W., Kim, G.-K., Koster, R.,
625 Lucchesi, R., Merkova, D., Nielsen, J. E., Partyka, G., Pawson, S., Putman, W., Rienecker, M., Schubert, S. D., Sienkiewicz, M., and Zhao, B.: The Modern-Era Retrospective Analysis for Research and Applications, Version 2 (MERRA-2), Journal of Climate, 30, 5419–5454, https://doi.org/10.1175/jcli-d-16-0758.1, 2017.

Gentine, P., Eyring, V., and Beucler, T.: Deep Learning for the Parametrization of Subgrid Processes in Climate Models, chap. 21, pp. 307–314, John Wiley & Sons, Ltd, Chichester, West Sussex, UK, https://doi.org/https://doi.org/10.1002/9781119646181.ch21, 2021.

630 Giorgetta, M. A., Brokopf, R., Crueger, T., Esch, M., Fiedler, S., Helmert, J., Hohenegger, C., Kornblueh, L., Köhler, M., Manzini, E., Mauritsen, T., Nam, C., Raddatz, T., Rast, S., Reinert, D., Sakradzija, M., Schmidt, H., Schneck, R., Schnur, R., Silvers, L., Wan, H., Zängl, G., and Stevens, B.: ICON-A, the Atmosphere Component of the ICON Earth System Model: I. Model Description, Journal of Advances in Modeling Earth Systems, 10, 1613–1637, https://doi.org/10.1029/2017ms001242, 2018.

Hersbach, H., Bell, B., Berrisford, P., Hirahara, S., Horányi, A., Muñoz-Sabater, J., Nicolas, J., Peubey, C., Radu, R., Schepers, D., Sim-
635 mons, A., Soci, C., Abdalla, S., Abellan, X., Balsamo, G., Bechtold, P., Biavati, G., Bidlot, J., Bonavita, M., Chiara, G. D., Dahlgren, P., Dee, D., Diamantakis, M., Dragani, R., Flemming, J., Forbes, R., Fuentes, M., Geer, A., Haimberger, L., Healy, S., Hogan, R. J., Hólm, E., Janisková, M., Keeley, S., Laloyaux, P., Lopez, P., Lupu, C., Radnoti, G., de Rosnay, P., Rozum, I., Vamborg, F., Villaume, S., and Thépaut, J.-N.: The ERA5 global reanalysis, Quarterly Journal of the Royal Meteorological Society, 146, 1999–2049, https://doi.org/10.1002/qj.3803, 2020.

640 Hourdin, F., Mauritsen, T., Gettelman, A., Golaz, J.-C., Balaji, V., Duan, Q., Folini, D., Ji, D., Klocke, D., Qian, Y., Rauser, F., Rio, C., Tomassini, L., Watanabe, M., and Williamson, D.: The Art and Science of Climate Model Tuning, Bulletin of the American Meteorological Society, 98, 589–602, https://doi.org/10.1175/bams-d-15-00135.1, 2017.

Hourdin, F., Williamson, D., Rio, C., Couvreux, F., Roehrig, R., Villefranque, N., Musat, I., Fairhead, L., Diallo, F. B., and Volodina, V.: Process-Based Climate Model Development Harnessing Machine Learning: II. Model Calibration From Single Column to Global, Journal
645 of Advances in Modeling Earth Systems, 13, https://doi.org/10.1029/2020ms002225, 2021.

Hourdin, F., Ferster, B., Deshayes, J., Mignot, J., Musat, I., and Williamson, D.: Toward machine-assisted tuning avoiding the underestimation of uncertainty in climate change projections, Science Advances, 9, https://doi.org/10.1126/sciadv.adf2758, 2023.

ICON: ICON: Icosahedral Nonhydrostatic Weather and Climate Model, https://code.mpimet.mpg.de/projects/iconpublic, 2015.

Iturbide, M., Gutiérrez, J. M., Alves, L. M., Bedia, J., Cerezo-Mota, R., Cimadevilla, E., Cofiño, A. S., Luca, A. D., Faria, S. H., Gorodet-
650 skaya, I. V., Hauser, M., Herrera, S., Hennessy, K., Hewitt, H. T., Jones, R. G., Krakovska, S., Manzanas, R., Martínez-Castro, D., Narisma, G. T., Nurhati, I. S., Pinto, I., Seneviratne, S. I., van den Hurk, B., and Vera, C. S.: An update of IPCC climate reference regions for subcontinental analysis of climate model data: definition and aggregated datasets, Earth System Science Data, 12, 2959–2970, https://doi.org/10.5194/essd-12-2959-2020, 2020.

Jorge Nocedal, S. J. W.: Numerical Optimization, Springer New York, https://doi.org/10.1007/978-0-387-40065-5, 2006.

655 Jungclaus, J. H., Lorenz, S. J., Schmidt, H., Brovkin, V., Brüggemann, N., Chegini, F., Crüger, T., De-Vrese, P., Gayler, V., Giorgetta, M. A., Gutjahr, O., Haak, H., Hagemann, S., Hanke, M., Ilyina, T., Korn, P., Kröger, J., Linardakis, L., Mehlmann, C., Mikolajewicz, U., Müller, W. A., Nabel, J. E. M. S., Notz, D., Pohlmann, H., Putrasahan, D. A., Raddatz, T., Ramme, L., Redler, R., Reick, C. H., Riddick, T., Sam, T., Schneck, R., Schnur, R., Schupfner, M., Storch, J.-S., Wachsmann, F., Wieners, K.-H., Ziemen, F., Stevens, B., Marotzke, J., and Claussen, M.: The ICON Earth System Model Version 1.0, Journal of Advances in Modeling Earth Systems, 14,
660 https://doi.org/10.1029/2021ms002813, 2022.

Karlsson, K.-G., Anttila, K., Trentmann, J., Stengel, M., Solodovnik, I., Meirink, J. F., Devasthale, A., Kothe, S., Jääskeläinen, E., Sedlar, J., Benas, N., van Zadelhoff, G.-J., Stein, D., Finkensieper, S., Håkansson, N., Hollmann, R., Kaiser, J., and Werscheck, M.: CLARA-A2.1: CM SAF cLoud, Albedo and surface RAdiation dataset from AVHRR data - Edition 2.1, https://doi.org/10.5676/EUM_SAF_CM/CLARA_AVHRR/V002_01, 2020.

665   Kato, S., Loeb, N. G., Rose, F. G., Doelling, D. R., Rutan, D. A., Caldwell, T. E., Yu, L., and Weller, R. A.: Surface Irradiances Consistent with CERES-Derived Top-of-Atmosphere Shortwave and Longwave Irradiances, Journal of Climate, 26, 2719–2740, https://doi.org/10.1175/jcli-d-12-00436.1, 2013.

Loeb, N. G., Wielicki, B. A., Doelling, D. R., Smith, G. L., Keyes, D. F., Kato, S., Manalo-Smith, N., and Wong, T.: Toward Optimal Closure of the Earth's Top-of-Atmosphere Radiation Budget, Journal of Climate, 22, 748–766, https://doi.org/10.1175/2008jcli2637.1, 2009.

670   Loeppky, J. L., Sacks, J., and Welch, W. J.: Choosing the Sample Size of a Computer Experiment: A Practical Guide, Technometrics, 51, 366–376, https://doi.org/10.1198/tech.2009.08040, 2009.

Mansfield, L. A. and Sheshadri, A.: Calibration and Uncertainty Quantification of a Gravity Wave Parameterization: A Case Study of the Quasi-Biennial Oscillation in an Intermediate Complexity Climate Model, Journal of Advances in Modeling Earth Systems, 14, https://doi.org/10.1029/2022ms003245, 2022.

675   Mauritsen, T., Stevens, B., Roeckner, E., Crueger, T., Esch, M., Giorgetta, M., Haak, H., Jungclaus, J., Klocke, D., Matei, D., Mikolajewicz, U., Notz, D., Pincus, R., Schmidt, H., and Tomassini, L.: Tuning the climate of a global model, Journal of Advances in Modeling Earth Systems, 4, n/a–n/a, https://doi.org/10.1029/2012ms000154, 2012.

Mignot, J., Hourdin, F., Deshayes, J., Boucher, O., Gastineau, G., Musat, I., Vancoppenolle, M., Servonnat, J., Caubel, A., Chéruy, F., Denvil, S., Dufresne, J.-L., Ethé, C., Fairhead, L., Foujols, M.-A., Grandpeix, J.-Y., Levavasseur, G., Marti, O., Menary, M.,
680   Rio, C., Rousset, C., and Silvy, Y.: The Tuning Strategy of IPSL-CM6A-LR, Journal of Advances in Modeling Earth Systems, 13, https://doi.org/10.1029/2020ms002340, 2021.

NASA/LARC/SD/ASDC: CERES Energy Balanced and Filled (EBAF) TOA and Surface Monthly means data in netCDF Edition 4.1, https://doi.org/10.5067/TERRA-AQUA/CERES/EBAF_L3B.004.1, 2019.

Rao, J., Garfinkel, C. I., White, I. P., and Schwartz, C.: The Southern Hemisphere Minor Sudden Stratospheric Warming in September 2019
685   and its Predictions in S2S Models, Journal of Geophysical Research: Atmospheres, 125, https://doi.org/10.1029/2020jd032723, 2020.

Rasmussen, C. E.: Gaussian processes for machine learning, MIT Press, https://gaussianprocess.org/gpml/chapters/RW.pdf, 2006.

Rasmussen, C. E. and Williams, C. K. I.: Gaussian Processes for Machine Learning, The MIT Press, https://doi.org/10.7551/mitpress/3206.001.0001, 2005.

Saltelli, A., Annoni, P., Azzini, I., Campolongo, F., Ratto, M., and Tarantola, S.: Variance based sensitivity analysis of model output. Design
690   and estimator for the total sensitivity index, Computer Physics Communications, 181, 259–270, https://doi.org/10.1016/j.cpc.2009.09.018, 2010.

Schmidt, G. A., Bader, D., Donner, L. J., Elsaesser, G. S., Golaz, J.-C., Hannay, C., Molod, A., Neale, R. B., and Saha, S.: Practice and philosophy of climate model tuning across six US modeling centers, Geoscientific Model Development, 10, 3207–3223, https://doi.org/10.5194/gmd-10-3207-2017, 2017.

695   Stengel, M., Stapelberg, S., Sus, O., Schlundt, C., Poulsen, C., Thomas, G., Christensen, M., Carbajal Henken, C., Preusker, R., Fischer, J., Devasthale, A., Willén, U., Karlsson, K.-G., McGarragh, G. R., Proud, S., Povey, A. C., Grainger, R. G., Meirink, J. F., Feofilov, A., Bennartz, R., Bojanowski, J. S., and Hollmann, R.: Cloud property datasets retrieved from AVHRR, MODIS, AATSR and MERIS in the framework of the Cloud cci project, Earth System Science Data, 9, 881–904, https://doi.org/10.5194/essd-9-881-2017, 2017.

Tebaldi, C., Debeire, K., Eyring, V., Fischer, E., Fyfe, J., Friedlingstein, P., Knutti, R., Lowe, J., O'Neill, B., Sanderson, B., van Vuuren,
700   D., Riahi, K., Meinshausen, M., Nicholls, Z., Tokarska, K. B., Hurtt, G., Kriegler, E., Lamarque, J.-F., Meehl, G., Moss, R., Bauer, S. E., Boucher, O., Brovkin, V., Byun, Y.-H., Dix, M., Gualdi, S., Guo, H., John, J. G., Kharin, S., Kim, Y., Koshiro, T., Ma, L., Olivié, D., Panickal, S., Qiao, F., Rong, X., Rosenbloom, N., Schupfner, M., Séférian, R., Sellar, A., Semmler, T., Shi, X., Song, Z., Steger, C.,

Stouffer, R., Swart, N., Tachiiri, K., Tang, Q., Tatebe, H., Voldoire, A., Volodin, E., Wyser, K., Xin, X., Yang, S., Yu, Y., and Ziehn, T.: Climate model projections from the Scenario Model Intercomparison Project (ScenarioMIP) of CMIP6, Earth System Dynamics, 12, 253–293, https://doi.org/10.5194/esd-12-253-2021, 2021.

Tripathi, O. P., Baldwin, M., Charlton-Perez, A., Charron, M., Eckermann, S. D., Gerber, E., Harrison, R. G., Jackson, D. R., Kim, B., Kuroda, Y., Lang, A., Mahmood, S., Mizuta, R., Roff, G., Sigmond, M., and Son, S.: The predictability of the extratropical stratosphere on monthly time-scales and its impact on the skill of tropospheric forecasts, Quarterly Journal of the Royal Meteorological Society, 141, 987–1003, https://doi.org/10.1002/qj.2432, 2014.

Watson-Parris, D., Williams, A., Deaconu, L., and Stier, P.: Model calibration using ESEm v1.1.0 – an open, scalable Earth system emulator, Geoscientific Model Development, 14, 7659–7672, https://doi.org/10.5194/gmd-14-7659-2021, 2021.

Williamson, D., Goldstein, M., Allison, L., Blaker, A., Challenor, P., Jackson, L., and Yamazaki, K.: History matching for exploring and reducing climate model parameter space using observations and a large perturbed physics ensemble, Climate Dynamics, 41, 1703–1729, https://doi.org/10.1007/s00382-013-1896-4, 2013.

Williamson, D. B., Blaker, A. T., and Sinha, B.: Tuning without over-tuning: parametric uncertainty quantification for the NEMO ocean model, Geoscientific Model Development, 10, 1789–1816, https://doi.org/10.5194/gmd-10-1789-2017, 2017.

Zhang, T., Li, L., Lin, Y., Xue, W., Xie, F., Xu, H., and Huang, X.: An automatic and effective parameter optimization method for model tuning, Geoscientific Model Development, 8, 3579–3591, https://doi.org/10.5194/gmd-8-3579-2015, 2015.

Zängl, G., Reinert, D., Rípodas, P., and Baldauf, M.: The ICON (ICOsahedral Non-hydrostatic) modelling frameworkof DWD and MPI-M: Description of the non-hydrostaticdynamical core, Quarterly Journal of the Royal Meteorological Society, 141, 563–579, https://doi.org/10.1002/qj.2378, 2014.
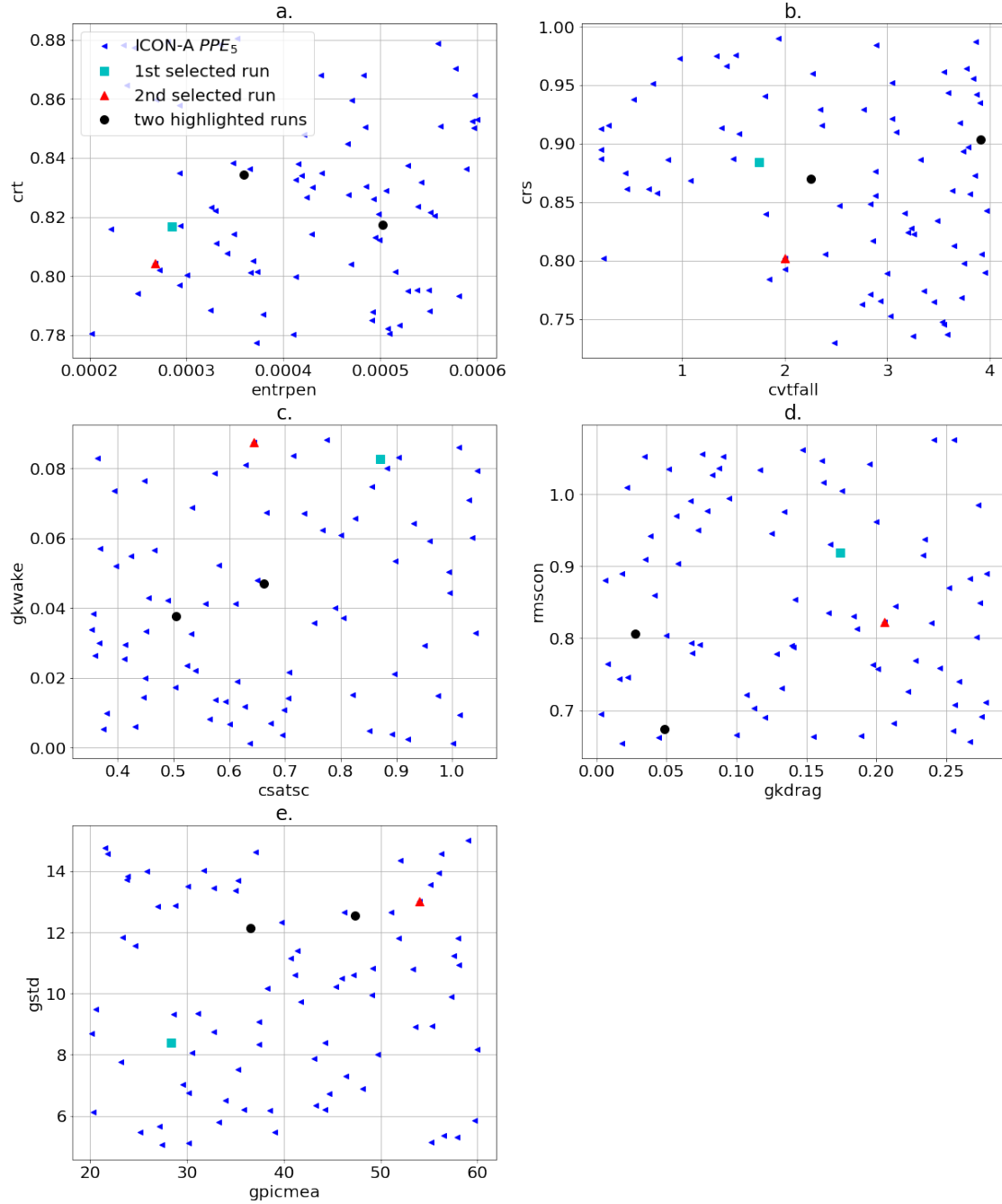
Figure C2. Sampled parameter values for PPE_5 (blue triangles). For each panel, two parameters are plotted on the two axes (see Tables 3 and 4). The PPE is generated with parameter set $\mathcal{P}_{\mathrm{pd}}$. Two selected PPE members corresponding to the best performing configurations are highlighted (cyan square and red triangle).
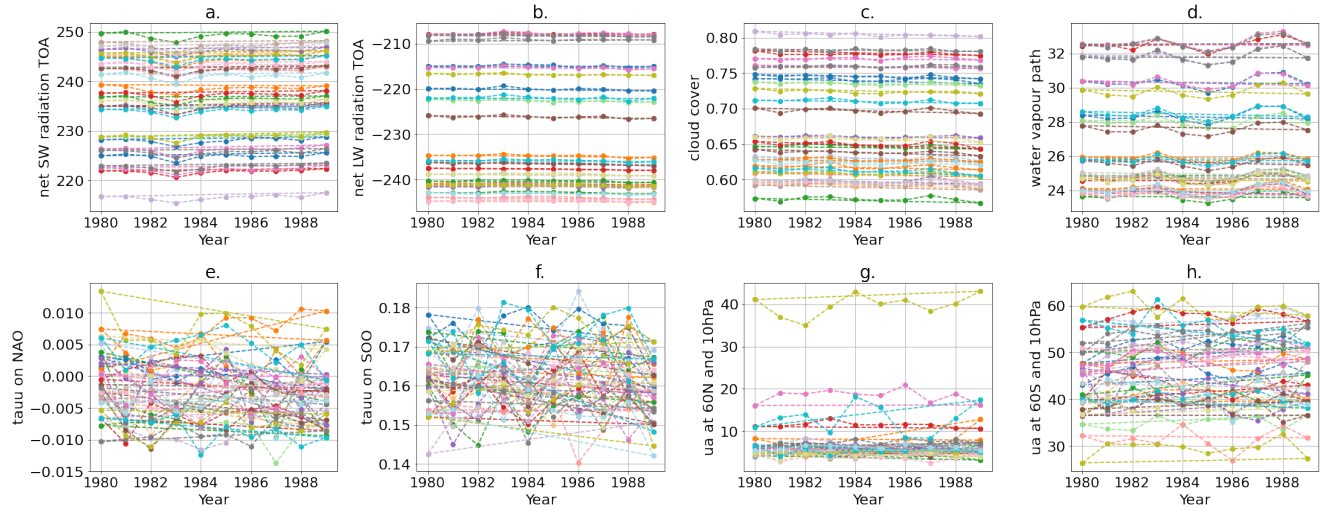
Figure D1. Time series (yearly averages) of the physics (top row, panels (a) to (d)) and dynamics (bottom row, panels (e) to (h)) output variables for 30 runs of PPE_5 (each color corresponds to one run). The values at year 1980 and 1989 are connected with a dashed line to help the reader identify the runs.
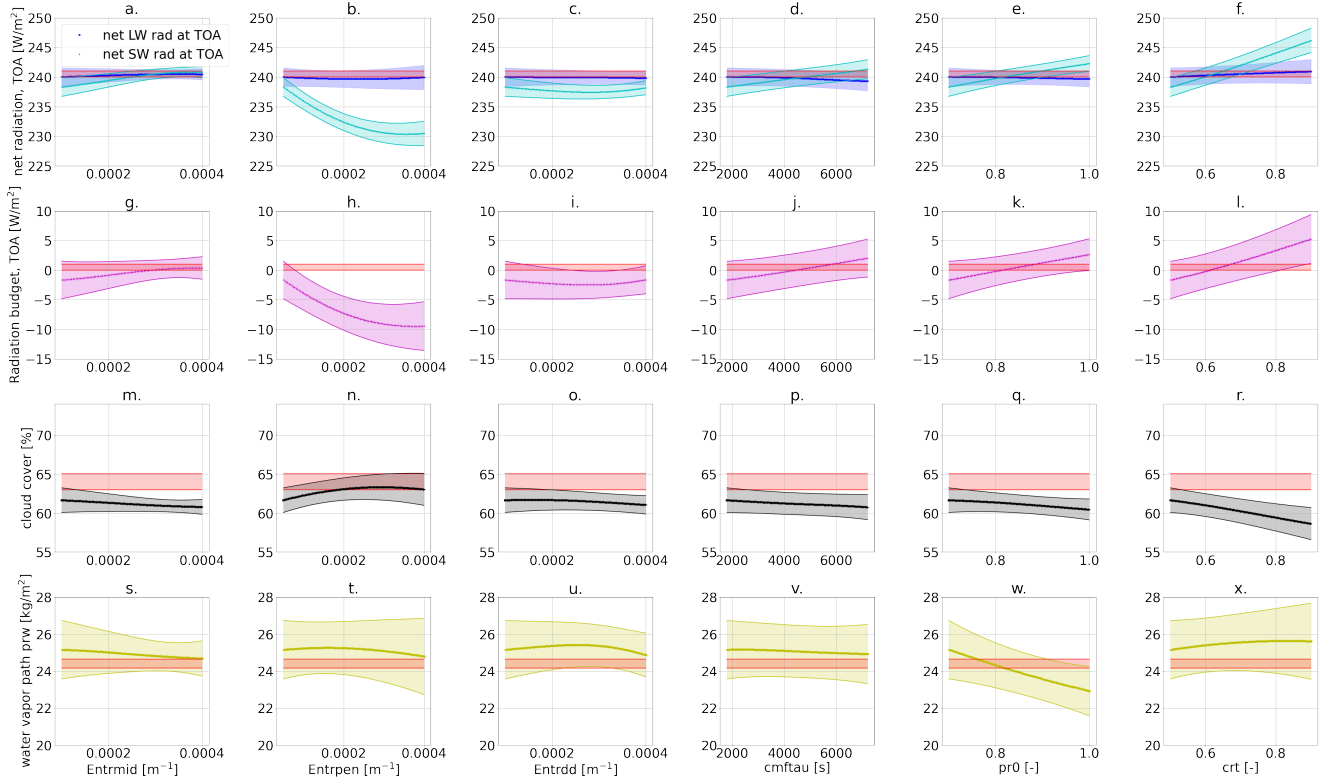
Figure E1. Parameter-to-output maps predicted with the GP-emulators trained on PPE_1 and PPE_2. Every column corresponds to one tuning parameter being changed (see the list in Table 3), and every row to an output metric. The parameters that are not being changed are kept fixed to their best performing value from PPE_2 (marked with the magenta star in Figures 2 and 3). The red shaded areas in each plot denote the allowed output ranges from the observational data. The other colored lines in each plot denote the emulator predictions (for the first row, dark and light blue denote the net long- and short-wave radiation at TOA, respectively), with the corresponding uncertainty (one standard deviation) represented as the shaded area.
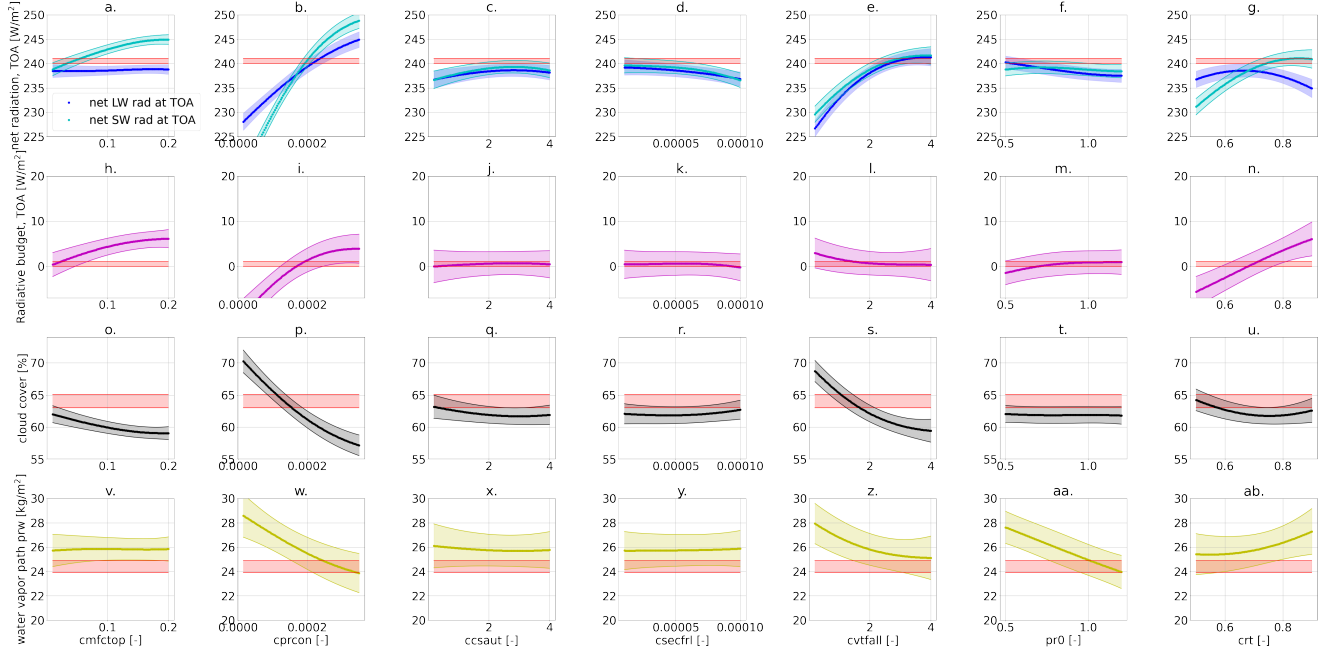
Figure E2. Parameter-to-output map predicted with the GP-emulators trained on PPE_3 and PPE_4. Every column corresponds to one tuning parameter being changed (see the list in Table 3), and every row to to an output variable. The parameters that are not being changed are kept fixed to their best performing value from PPE_2 (marked with the magenta star in Figures 2 and 3). The red shaded areas in each plot denote the allowed output ranges from the observational data. The other colored lines in each plot denote the emulator predictions (for the first row, dark and light blue denote the net long- and short-wave radiation at TOA, respectively), with the corresponding uncertainty (one standard deviation) represented as the shaded area.